CALCULATION OF GENERAL QUASISTATIONARY FIELDS IN THE PRESENCE OF AXISYMMETRIC CONDUCTORS

By

D. H. R. Suriyaarachchi

A Thesis
Submitted to the Faculty of Graduate Studies
in Partial Fulfilment of the Requirement
For the Degree of
Master of Science

Department of Electrical and Computer Engineering
University of Manitoba
Winnipeg, Manitoba

THE UNIVERSITY OF MANITOBA

FACULTY OF GRADUATE STUDIES

*****

COPYRIGHT PERMISSION

CALCULATION OF GENERAL QUASISTATIONARY FIELDS IN THE PRESENCE OF AXISYMMETRIC CONDUCTORS

BY

D.H.R. Suriyaarachchi

A Thesis/Practicum submitted to the Faculty of Graduate Studies of The University of Manitoba in partial fulfillment of the requirement of the degree

MASTER OF SCIENCE

THE UNIVERSITY OF MANITOBA
FACULTY OF GRADUATE STUDIES
*****
COPYRIGHT PERMISSION

CALCULATION OF GENERAL QUASISTATIONARY FIELDS IN THE PRESENCE OF AXISYMMETRIC CONDUCTORS

by
D. H. R. Suriyaarachchi

A Thesis/Practicum submitted to the Faculty of Graduate Studies of The University of Manitoba in partial fulfillment of the requirement of the degree of

Master of Science

To my parents.

Table of Contents

List of Tables

List of Figures

Acknowledgements

This thesis is the outcome of two years of hard work and struggle. I may have not made it through if I have not got the support of some wonderful people throughout this period. It's an honor for me to extend my warm acknowledgments to all of them at this point.

First of all, I would like to express my sincere gratitude to my advisor, Prof. Ioan R. Ciric, for suggesting me this topic and for his invaluable guidance, support and encouragement throughout this work. It has been a great privilege to work with him. I would also like to thank my examining committee for graciously accepting to review my thesis. Conducting this work would not have been possible without the financial support from Prof. Ciric's research grant and from the government of Manitoba in the form of a Graduate Scholarship. I would like to thank all my friends for their support and for making my stay in Winnipeg enjoyable. My special thanks goes to Mr. Nandaka Jayasekera for his help throughout my research work and for his suggestions in writing this thesis.

I am forever indebted to my family, especially to my parents for all their love and guidance throughout my life. Without them, I won't be the person who I am today. I am also grateful to my brother and sister for all their support. Last but not least, I would like to thank my loving Erandi for her patience, understanding and encouragements whenever I most needed them.

Hiranya Suriyaarachchi
February 27, 2008

Abstract

An efficient numerical method is presented for the solution of the integral equation satisfied by the current density induced in axisymmetric solid conductors immersed in given magnetic fields. The associated matrix equation is formulated by applying the method of moments with the unknown current density expanded in a Fourier series in the azimuthal angle, its coefficients being vector functions whose components along the meridian and azimuth directions only depend on the meridian coordinate.

Illustrative numerical results are generated for conducting prolate and oblate spheroids in the presence of axially directed uniform fields, for prolate and oblate spheroids and spheres in the presence of arbitrarily directed uniform fields and, also, in fields produced by current-carrying turns. The generated numerical results are compared with available analytical results to investigate their accuracy. The efficiency of using pulse basis functions and impulse basis functions is also investigated.

Chapter 1

Introduction

1.1 Overview and Objective

Many engineering applications such as induction heating, levitation, eddy-current breaking, electromagnetic shielding, nondestructive testing, require the analysis of the currents induced in a solid conductor in the presence of a quasistationary magnetic field. In quasistationary regime, the displacement current is negligible compared to the conduction current and the field quantities satisfy the Helmholtz equation inside the conductor. An accurate study requires the determination of the field quantities both inside and outside the conductor.

An exact analytical solution of the quasistationary electromagnetic fields in the presence of conducting bodies is only possible in just a few cases. In [1], such a solution is presented for a sphere in the presence of a coaxial current-carrying turn. The exact solution for the magnetic field has been presented in [2] for conducting spheroids in the presence of coaxial current-carrying turns using the method of separation of variables. Magnetic dipole moments have been calculated for a conducting and permeable spheroid with uniform axial excitations in [3], and in [4] for transverse excitations.

By employing approximate boundary conditions, various systems containing given induced conductors can be analyzed using only the fields outside them. The most widely used approximate boundary condition is the standard impedance boundary condition (SIBC), which can be applied when the penetration depths of the fields are relatively small compared to the dimensions of the object. The SIBC states that the ratio between the tangential components of the electric and magnetic field intensities at the conductor boundary is equal to the intrinsic impedance of the medium in which the fields penetrate. At higher frequencies, the induced currents in the conductor can be assumed to be confined to their surface and, then, the perfect electric conductor (PEC) boundary condition can be applied with sufficient accuracy. The tangential electric field on the surface of the conductor is assumed to be zero in the PEC model. The accuracy of the PEC model and the SIBC model has been studied in [5] and it has been found that, for spherical conductors the power losses and forces calculated using the SIBC model introduce a maximum percentage error of less than 1% with respect to the exact solution when the skin depths are less than 1/10 of the radius, while the PEC model requires the skin depths to be less than 1/35 to have the same accuracy. In [6], a similar study has been performed for conducting spheroids. The validity of the PEC model has been analyzed in [7] for spheroids with various axial ratios by comparing the computed results with experimental data.

An exact analytical solution is possible for certain axisymmetric systems, when both the object and the inducing field are axisymmetric. When either the shape of the object or the outside field is arbitrary, an analytical solution is, in general, not possible. For a numerical solution, an integral equation representation of the boundary value problem is usually more advantageous than the partial differential equation representation. The errors at various observation points may partially cancel each other in the summation process when employing integral equations whereas, in general, they may propagate along successive steps when using partial differential equations. The most frequently used method to obtain an integral equation from the partial differential equation is to use an associated Green's function, obtained from a standard boundary value problem [8].

Two frequently used numerical techniques are the finite element method and the method of moments. The finite element method is more versatile and powerful, being applicable to more complex problems, while the method of moments is conceptually more simple and easy to implement numerically. The method of moments is widely used [9], [10] to solve a variety of electromagnetic problems such as radiation, scattering, analysis of antenna beam patterns, microstrips, quasistationary electromagnetic problems, etc. The procedure of applying the method of moments involves the conversion (discretization) of the integral equation using a set of basis and weighting functions, and the solution of a matrix equation.

In this thesis, we calculate quasistationary magnetic fields in the presence of bodies of revolution using the perfect conductor model. In the general case of arbitrarily shaped conductors, the entire conductor surface has to be discretized, which requires a large number of computations to be performed. In order to reduce substantially the amount of computation required, we exploit the axisymmetry of the geometry of the conducting body, even when the inducing fields are not axisymmetric with respect to the body axis of revolution. Namely, the induced surface current density is represented in the form of a Fourier series in the azimuthal angle, with its coefficients being the components of the current density along the meridian and azimuth directions, and only depending on the meridian coordinate [11].

1.2 Thesis Outline

In Chapter 2, an integral equation is derived for the induced surface current density for a conducting object in an arbitrary external magnetic field. A matrix equation is derived by applying the method of moments. Details of the derivation of matrix elements for axisymmetric bodies in arbitrary inducing fields are presented for impulse weighting functions and for both pulse and impulse basis functions.

We present in Chapter 3, details of the computation of the matrix elements and numerical results for the normalized tangential magnetic field intensity on the surface of the spheroids in the presence of an axially directed uniform magnetic field and in the field produced by coaxial circular current-carrying turns. Results for spheres in the vicinity of a coaxial circular current-carrying turn are also presented as a special case. The efficiency of using various types of basis functions to compute the induced surface current density has been investigated by comparing the results obtained with impulse basis functions and with pulse basis functions. The effect of the number of basis functions on the convergence of the normalized tangential magnetic field intensity at the middle of the meridian line has also been studied. We compare the generated numerical results with the analytical results in [7] by evaluating the percentage error between them.

Chapter 4 consists of the details of the computation of the matrix equation elements for a uniform inducing magnetic field directed at an arbitrary angle with respect to the axis of symmetry of the body and for an external field produced by circular current-carrying turns whose axes are shifted with respect to the axis of revolution of the body. Numerical results for the normalized tangential magnetic fields on the surface of the spheres and spheroids are presented. In the case of spheres, the uniform field is directed at an arbitrary angle with respect to the reference $z-$axis and the circular turn axis is shifted with respect to the same axis. For spheres, the generated numerical results are compared with those from the analytical solution by indicating the percentage error. Conclusions and suggestions for future work are presented in Chapter 5.

In Appendix A, we present details of the derivation of the analytical solution for the magnetic field at the surface of perfect conducting spheroids in the presence of a coaxial current-carrying circular turn. The analytical solutions corresponding to the cases of spheroids in axially directed uniform fields and to spheres in the presence of circular-current carrying turns are derived as special cases.

Details of the analytical solution for the tangential magnetic field at the surface of a perfect conducting sphere in an uniform field directed at an arbitrary angle with respect to a reference z-axis are given in Appendix B.

Chapter 2

General Formulation

2.1 Integral Equation for Eddy Currents on an Arbitrarily Shaped Perfect Conducting Body in a Given Magnetic Field

Consider an arbitrarily shaped conductor in an external magnetic field $\boldsymbol{H}_{inc}$ as shown in Fig. 2.1, where P is the observation point and the position vectors of the source and observation points are $\boldsymbol{r}$ and $\boldsymbol{r}'$, respectively. The total magnetic field intensity at an observation point outside the conductor, $\boldsymbol{H}(\boldsymbol{r})$ can be written as

$$\boldsymbol{H}(\boldsymbol{r}) = \boldsymbol{H}_{inc}(\boldsymbol{r}) + \boldsymbol{H}_{ind}(\boldsymbol{r}), \tag{2.1}$$

where $\boldsymbol{H}_{ind}(\boldsymbol{r})$ is the magnetic field intensity due to the induced currents on the conducting body. By applying the Biot-Savart law, we have

$$\boldsymbol{H}_{ind}(\boldsymbol{r}) = \frac{1}{4\pi}\int_S \boldsymbol{J}_s(\boldsymbol{r}') \times \frac{\boldsymbol{R}}{R^3} ds', \tag{2.2}$$

where $\boldsymbol{R} = \boldsymbol{r} - \boldsymbol{r}'$ and $\boldsymbol{J}_s$ is the density of the current induced on the conductor.

To apply the boundary condition at the conductor surface, observation is made just outside the body. At a point on the boundary between the two media, the tangential magnetic field is discontinuous by the amount of the current density induced on

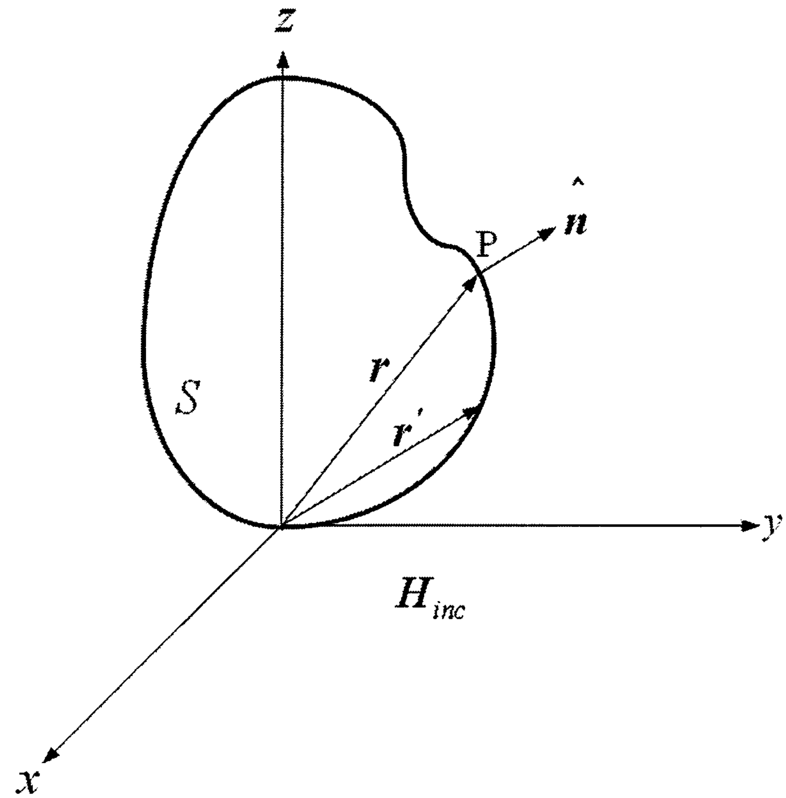

Figure 2.1: An arbitrary shaped conductor in an external magnetic field.

the surface of the conductor. If the conductor is assumed to be perfect, the magnetic field inside is zero. Therefore, an integral equation for the surface current density can be formulated in the form

$$\boldsymbol{J}_s(\boldsymbol{r}) - \hat{\boldsymbol{n}} \times \frac{1}{4\pi} \int_S \boldsymbol{J}_s(\boldsymbol{r}') \times \frac{\boldsymbol{R}}{R^3} ds' = \hat{\boldsymbol{n}} \times \boldsymbol{H}_{inc}(\boldsymbol{r}), \qquad \boldsymbol{r} \in S, \tag{2.3}$$

where $\hat{\boldsymbol{n}}$ is the outwardly oriented unit vector normal to the surface S at point P. When the observation point coincides with the source point, R is zero yielding a singularity in the integral of (2.3).

The integral equation is evaluated numerically by dividing the conductor surface into patches. A part of the induced magnetic field is produced by the self patch and the rest is produced by all the other patches. It is assumed that the self patch becomes a flat surface as the size of the segment becomes small. Therefore, the scattered magnetic field intensity from the self patch is

$$\boldsymbol{H}_{ind,self}(\boldsymbol{r}) = -\frac{1}{2}\hat{\boldsymbol{n}} \times \boldsymbol{J}_s(\mathrm{r}). \tag{2.4}$$

The contribution from the non-self patches to the scattered magnetic field intensity is

$$\boldsymbol{H}_{ind,non\ self}(\boldsymbol{r}) = \frac{1}{4\pi} \fint_S \boldsymbol{J}_s(\boldsymbol{r}') \times \frac{\boldsymbol{R}}{R^3} ds', \tag{2.5}$$

where the integral is taken in principal value. Substituting (2.4) and (2.5) into (2.3) modifies the integral equation such that

$$\frac{1}{2}\boldsymbol{J}_s(\boldsymbol{r}) - \frac{1}{4\pi}\hat{\boldsymbol{n}} \times \fint_S \boldsymbol{J}_s(\boldsymbol{r}') \times \frac{\boldsymbol{R}}{R^3} ds' = \boldsymbol{H}'_{inc}(\boldsymbol{r}), \qquad \boldsymbol{r} \in S, \tag{2.6}$$

with $\boldsymbol{H}'_{inc}(\boldsymbol{r}) = \hat{\boldsymbol{n}} \times \boldsymbol{H}_{inc}(\boldsymbol{r})$.

Once a solution is obtained for the current density $\boldsymbol{J}_s$, the total magnetic field intensity outside the conductor can be obtained easily form (2.1) and (2.2).

2.2 Methods of Solution

2.2.1 Method of Moments for Arbitrarily Shaped Bodies

The integral equation (2.6) can be written as

$$L(\boldsymbol{J}_s) = \boldsymbol{H}'_{inc}(\boldsymbol{r}), \tag{2.7}$$

where the L is a linear operator,

$$L(\boldsymbol{J}_s) = \frac{1}{2}\boldsymbol{J}_s(\boldsymbol{r}) - \frac{1}{4\pi}\hat{\boldsymbol{n}} \times \fint_S \boldsymbol{J}_s(\boldsymbol{r}') \times \frac{\boldsymbol{R}}{R^3} ds'. \tag{2.8}$$

Using the method of moments (2.7) can be converted to a matrix equation. Namely, $\boldsymbol{J}_s$ is expanded in a series of basis functions and an inner product is taken with a set of weighting functions $\boldsymbol{W}_i(\boldsymbol{r})$ [10],

$$\langle \boldsymbol{W}_i(\boldsymbol{r}), L(\boldsymbol{J}_s(\boldsymbol{r}))\rangle = \langle \boldsymbol{W}_i(\boldsymbol{r}), \boldsymbol{H}'_{inc}(\boldsymbol{r})\rangle, \tag{2.9}$$

where

$$\langle \boldsymbol{W}, \boldsymbol{J}\rangle \triangleq \int_S \boldsymbol{W} \cdot \boldsymbol{J} ds. \tag{2.10}$$

The surface current density is expanded in a series of basis functions $\mathbf{f}_k(\boldsymbol{r})$ as

$$\boldsymbol{J}_s(\boldsymbol{r}) = \sum_{k=1}^{\infty} I_k \boldsymbol{f}_k(\boldsymbol{r}), \tag{2.11}$$

where I_k are constants to be determined. Making use of the linearity of L, the resulting equation after substituting (2.11) into (2.9), can be written as

$$\sum_{k=1}^{\infty} I_k \langle \boldsymbol{W}_i(\boldsymbol{r}), L(\boldsymbol{f}_k(\boldsymbol{r}))\rangle = \langle \boldsymbol{W}_i(\boldsymbol{r}), \boldsymbol{H}'_{inc}(\boldsymbol{r})\rangle, \qquad i = 1, 2, 3, \cdots. \tag{2.12}$$

The equation (2.12) can be expressed in matrix form as

$$[Z][I] = [V], \tag{2.13}$$

where $(Z)_{ik} = \langle \boldsymbol{W}_i(\boldsymbol{r}), L(\boldsymbol{f}_k(\boldsymbol{r}))\rangle$, $(V)_i = \langle \boldsymbol{W}_i(\boldsymbol{r}), \boldsymbol{H}'_{inc}(\boldsymbol{r})\rangle$ and $[I]$ contains the coefficients I_k to be determined. $[Z]$ is called the impedance matrix and $[V]$ the inducing field matrix.

All the expressions derived so far are valid for bodies of arbitrary shape. Since the scope of this thesis is limited to bodies which are symmetric about an axis of rotation, here after the focus will be only on bodies of revolution.

2.2.2 Moment Method for Axisymmetric Bodies

A conducting body of revolution is shown in Fig. 2.2. (ρ, ϕ, z) are the circular cylindrical coordinate variables and t is a length variable along the meridian C. The unit vectors $(\hat{\boldsymbol{n}}, \hat{\boldsymbol{\phi}}, \hat{\boldsymbol{t}})$ forms an orthogonal right-handed triad. $\hat{\boldsymbol{n}}$ is the unit vector oriented along the outward normal to the surface S of the body while $\hat{\boldsymbol{\phi}}$ and $\hat{\boldsymbol{t}}$ are tangential to the surface S.

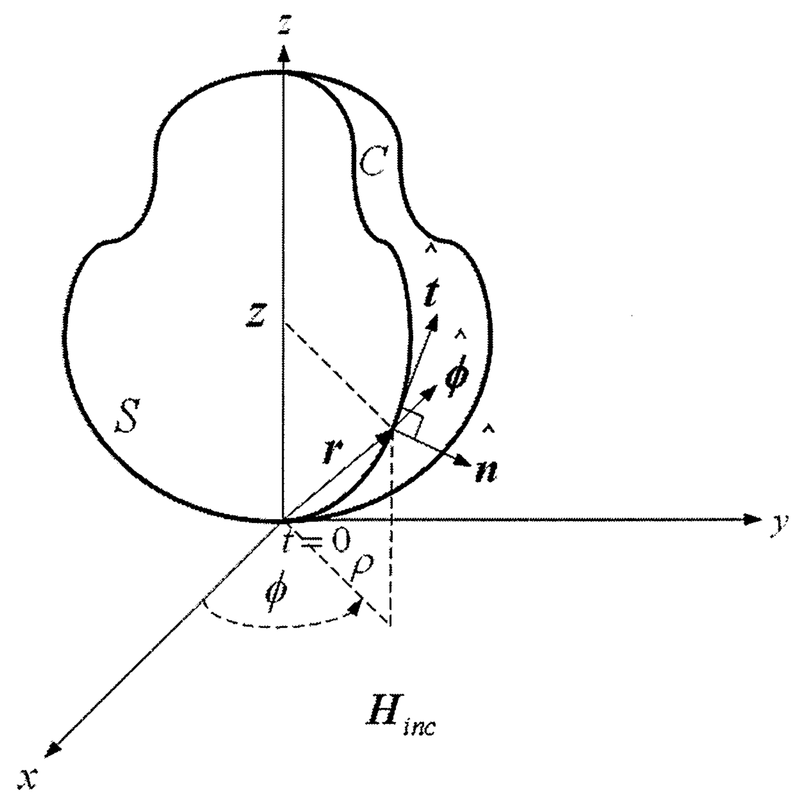

Figure 2.2: Geometry of the axisymmetric conductor.

The induced surface current density and $\boldsymbol{H}'_{inc}$ in (2.6) can be written in terms of the local coordinate variables (t, ϕ) and of the unit vectors $(\hat{\boldsymbol{t}}, \hat{\boldsymbol{\phi}})$ as

$$\boldsymbol{J}_s(t,\phi) = \sum_{k=1}^{\infty} \left[I_k^t f_k(t,\phi)\hat{\boldsymbol{t}} + I_k^\phi f_k(t,\phi)\hat{\boldsymbol{\phi}} \right] \tag{2.14}$$

and

$$\boldsymbol{H}'_{inc}(t,\phi) = \boldsymbol{H}'^{t}_{inc}(t,\phi)\hat{\boldsymbol{t}} + \boldsymbol{H}'^{\phi}_{inc}(t,\phi)\hat{\boldsymbol{\phi}}, \tag{2.15}$$

respectively. The superscripts t and ϕ in the coefficients I_k^t and I_k^ϕ, and in H'^{t}_{inc} and H'^{ϕ}_{inc} indicate the direction. Because of the rotational symmetry of the body, the induced surface current density as well as the inducing field on the body surface have a 2π periodicity in the azimuthal angle. Therefore, both the surface current density and the non-axisymmetric inducing field are expanded in Fourier series as

$$\boldsymbol{J}_s(t,\phi) = \sum_{m=-\infty}^{\infty} \sum_{k=1}^{\infty} (I_{mk}^t \boldsymbol{J}_{mk}^t + I_{mk}^\phi \boldsymbol{J}_{mk}^\phi), \tag{2.16}$$

$$\boldsymbol{H}'_{inc}(t,\phi) = \sum_{m=-\infty}^{\infty} \boldsymbol{H}'_{inc,m}(t) e^{jm\phi}, \tag{2.17}$$

where $\mathbf{J}_{mk}^t = \hat{\boldsymbol{t}} f_k(t) e^{jm\phi}$, $\mathbf{J}_{mk}^\phi = \hat{\boldsymbol{\phi}} f_k(t) e^{jm\phi}$ and $\boldsymbol{H}'_{inc,m}(t) = \frac{1}{2\pi} \int_0^{2\pi} \boldsymbol{H}'_{inc}(t,\phi) e^{-jm\phi}$. This allows us to use only segments along the meridian line C, instead of the patches over the entire conductor surface. We divide the meridian into N number of segments.

We choose weighting functions of the form

$$\boldsymbol{W}_{ni}^t(t,\phi) = \hat{\boldsymbol{t}} w_i(t) e^{-jn\phi} \qquad \text{and} \qquad \boldsymbol{W}_{ni}^\phi(t,\phi) = \hat{\boldsymbol{\phi}} w_i(t) e^{-jn\phi}, \tag{2.18}$$

where $w_i(t)$ are functions to be selected.

Substitution of (2.16), (2.17), and (2.18) into (2.9) results in a decoupling of the Fourier modes. Furthermore, the resulting set of equations can be expressed as a matrix equation with partitioned matrices;

$$\begin{bmatrix} [Z_n^{tt}] & [Z_n^{t\phi}] \\ [Z_n^{\phi t}] & [Z_n^{\phi\phi}] \end{bmatrix} \begin{bmatrix} [I_n^t] \\ [I_n^\phi] \end{bmatrix} = \begin{bmatrix} [V_n^t] \\ [V_n^\phi] \end{bmatrix}, \tag{2.19}$$

with the elements

$$\begin{aligned} \left(Z_n^{tt}\right)_{ik} &= \langle \boldsymbol{W}_{ni}^t, L(\boldsymbol{J}_{nk}^t)\rangle \quad , \quad \left(Z_n^{t\phi}\right)_{ik} = \langle \boldsymbol{W}_{ni}^t, L(\boldsymbol{J}_{nk}^\phi)\rangle, \\ \left(Z_n^{\phi t}\right)_{ik} &= \langle \boldsymbol{W}_{ni}^\phi, L(\boldsymbol{J}_{nk}^t)\rangle \quad , \quad \left(Z_n^{\phi\phi}\right)_{ik} = \langle \boldsymbol{W}_{ni}^\phi, L(\boldsymbol{J}_{nk}^\phi)\rangle, \end{aligned} \tag{2.20}$$

$$\left(V_n^t\right)_i = \langle \boldsymbol{W}_{ni}^t, \boldsymbol{H}_{inc,n}'(t)e^{jn\phi}\rangle \quad \text{and} \quad \left(V_n^\phi\right)_i = \langle \boldsymbol{W}_{ni}^\phi, \boldsymbol{H}_{inc,n}'(t)e^{jn\phi}\rangle. \tag{2.21}$$

2.3 Evaluation of Matrix Elements

To demonstrate the calculation of impedance matric elements, consider $(Z_n^{tt})_{ik}$ in (2.20) which can be expanded as

$$\begin{aligned} \left(Z_n^{tt}\right)_{ik} =& \frac{1}{2}\int_S w_i(t) f_k(t) ds - \frac{1}{4\pi}\int_S w_i(t)\hat{\boldsymbol{t}} \cdot \left[\hat{\boldsymbol{n}} \times \fint_S f_k(t')\hat{\boldsymbol{t}}' \right. \\ & \left. \times \frac{\boldsymbol{R}}{R^3} e^{jn(\phi'-\phi)} ds ds' \right]. \end{aligned} \tag{2.22}$$

We express $\boldsymbol{R}/R^3$ and the local unit vectors in terms of the cartesian coordinate unit vectors. Then,

$$\frac{\boldsymbol{R}}{R^3} = \frac{(\rho\cos\phi - \rho'\cos\phi')\hat{\boldsymbol{x}} + (\rho\sin\phi - \rho'\sin\phi')\hat{\boldsymbol{y}} + (z-z')\hat{\boldsymbol{z}}}{[\rho^2 + \rho'^2 - 2\rho\rho'\cos(\phi-\phi') + (z-z')^2]^{\frac{3}{2}}} \tag{2.23}$$

and

$$\begin{aligned} \hat{\boldsymbol{t}} &= \sin\alpha\cos\phi\hat{\boldsymbol{x}} + \sin\alpha\sin\phi\hat{\boldsymbol{y}} + \cos\alpha\hat{\boldsymbol{z}}, \\ \hat{\boldsymbol{t}}' &= \sin\alpha'\cos\phi'\hat{\boldsymbol{x}} + \sin\alpha'\sin\phi'\hat{\boldsymbol{y}} + \cos\alpha'\hat{\boldsymbol{z}}, \\ \hat{\boldsymbol{\phi}} &= -\sin\phi\hat{\boldsymbol{x}} + \cos\phi\hat{\boldsymbol{y}}, \\ \hat{\boldsymbol{\phi}}' &= -\sin\phi'\hat{\boldsymbol{x}} + \cos\phi'\hat{\boldsymbol{y}}, \\ \hat{\boldsymbol{n}} &= \cos\alpha\cos\phi\hat{\boldsymbol{x}} + \cos\alpha\sin\phi\hat{\boldsymbol{y}} - \sin\alpha\hat{\boldsymbol{z}}, \end{aligned} \tag{2.24}$$

where α is the angle between $\hat{\boldsymbol{z}}$ and $\hat{\boldsymbol{t}}$ at the observation point P. It is defined to be positive if $\hat{\boldsymbol{t}}$ is directed away from the z-axis and is given by

$$\alpha = \tan^{-1}\left(\frac{-\hat{\boldsymbol{z}}\cdot\hat{\boldsymbol{n}}}{\hat{\boldsymbol{x}}\cdot\hat{\boldsymbol{n}}}\right)\bigg|_P . \tag{2.25}$$

Similarly, α' is defined with respect to $\hat{\boldsymbol{z}}$ and $\hat{\boldsymbol{t}}'$.

For axisymmetric bodies,

$$\int_S ds = \int_C \int_0^{2\pi} \rho dt d\phi. \tag{2.26}$$

After substituting (2.23), (2.24) and (2.26) into (2.22), we obtain finally

$$\begin{aligned}(Z_n^{tt})_{ik} =& \frac{1}{2}\int_C\int_0^{2\pi} w_i(t) f_k(t) \rho dt d\phi + \frac{1}{4\pi}\int_C\int_0^{2\pi} \fint_C \fint_0^{2\pi} w_i(t) f_k(t') \\ &\cdot \frac{\{\rho\cos\alpha' - [\rho'\cos\alpha' + (z-z')\sin\alpha']\}}{[\rho^2+\rho'^2-2\rho\rho'\cos(\phi-\phi')+(z-z')^2]^{\frac{3}{2}}} e^{jn(\phi'-\phi)}\rho\rho' dt dt' d\phi d\phi'.\end{aligned} \tag{2.27}$$

With the observations made at $\phi = 0$, the integrand in (2.27) becomes independent of ϕ. Therefore, the ϕ integration reduces to 2π. Defining

$$g_n \equiv \int_0^{\pi} \frac{\cos\, n\phi'}{R_0^3}\, d\phi', \tag{2.28}$$

where $R_0 = [\rho^2 + \rho'^2 - 2\rho\rho'\cos\phi' + (z-z')]^{\frac{1}{2}}$, these matrix elements become

$$\begin{aligned}(Z_n^{tt})_{ik} =& \pi\int_C w_i(t) f_k(t)\rho dt - \frac{1}{2}\int_C \fint_C w_i(t) f_k(t')\{2g_n\rho\cos\alpha' \\ &- [\rho'\cos\alpha' + (z-z')\sin\alpha'](g_{n+1}+g_{n-1})\}\rho\rho' dt dt'.\end{aligned} \tag{2.29}$$

Similarly, the remaining impedance matrix elements can be derived as

$$\left(Z_n^{t\phi}\right)_{ik} = \frac{1}{2j}\int_C \fint_C w_i(t) f_k(t')(z-z')(g_{n+1}-g_{n-1})\rho\rho' dt dt',$$

$$\begin{aligned}\left(Z_n^{\phi t}\right)_{ik} &= \frac{1}{2j}\int_C \fint_C w_i(t) f_k(t')[\rho\cos\alpha\sin\alpha' - \rho'\sin\alpha\cos\alpha' \\ &\quad -(z-z')\sin\alpha\sin\alpha'](g_{n+1}-g_{n-1})\rho\rho' dt dt',\end{aligned} \tag{2.30}$$

$$\begin{aligned}\left(Z_n^{\phi\phi}\right)_{ik} &= \pi\int_C w_i(t) f_k(t)\rho dt - \frac{1}{2}\int_C \fint_C w_i(t) f_k(t')\{-2g_n\rho'\cos\alpha \\ &\quad +[\rho\cos\alpha - (z-z')\sin\alpha](g_{n+1}+g_{n-1})\}\rho\rho' dt dt'.\end{aligned}$$

The inducing field matrix elements in (2.21) are obtained from

$$\begin{aligned}\left(V_n^t\right)_i &= 2\pi\int_C w_i(t) H_{inc,n}'^{t}(t)\rho dt \qquad \text{and} \\ \left(V_n^\phi\right)_i &= 2\pi\int_C w_i(t) H_{inc,n}'^{\phi}(t)\rho dt,\end{aligned} \tag{2.31}$$

where the superscript t or ϕ on $H_{inc,n}'$ indicates the direction, and $H_{inc,n}'^{t}$ and $H_{inc,n}'^{\phi}$ are the n-th Fourier modes of $H_{inc}'^{t}$ and $H_{inc}'^{\phi}$, respectively.

The impedance matrix depends on the geometric parameters of the body, the weighting functions and the basis functions while the inducing field matrix is determined by the external field. Let us now show the evaluation of the matrix elements with the specified weighting and basis functions. In what follows we always use impulses as weighting functions and impulses, as well as pulses as basis functions.

2.3.1 Matrix Elements with Impulse Weighting Functions and Impulse Basis Functions

When impulses placed at the center of the segments along C are used as basis functions, it is assumed that the surface current is concentrated only at the middle of

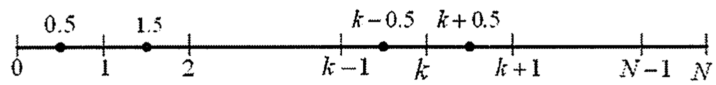

Figure 2.3: Meridian line divided into N number of segments.

each segment. Thus,

$$f_k(t) = \delta(t - t_k), \qquad\qquad w_i(t) = \delta(t - t_i), \tag{2.32}$$

where $\delta(t - t_k)$ and $\delta(t - t_i)$ are the Dirac delta functions, $t_k = k - 0.5$, $t_i = i - 0.5$, and $k, i = 1, 2, ..., N$. In all the numerical computations performed in this thesis, we have scaled the size of the body so that the length of each segment is one unit as shown in Fig. 2.3.

With this choice of functions, we can easily calculate the impedance and inducing matrix elements as

$$\begin{aligned}
\left(Z_n^{tt}\right)_{ik} &= \pi\rho_{t_i} - \frac{1}{2}\{2G_n\rho_{t_i}\cos\alpha'_{t_k} - [\rho'_{t_k}\cos\alpha'_{t_k} + (z_{t_i} - z'_{t_k})\sin\alpha'_{t_k}] \\
&\quad \cdot(G_{n+1} + G_{n-1})\}\rho_{t_i}\rho'_{t_k}, \\
\\
\left(Z_n^{t\phi}\right)_{ik} &= \frac{1}{2j}(z_{t_i} - z'_{t_k})(G_{n+1} - G_{n-1})\rho_{t_i}\rho'_{t_k}, \\
\\
\left(Z_n^{\phi t}\right)_{ik} &= \frac{1}{2j}[\rho_{t_i}\cos\alpha_{t_i}\sin\alpha'_{t_k} - \rho'_{t_k}\sin\alpha_{t_i}\cos\alpha'_{t_k} \\
&\quad -(z_{t_i} - z'_{t_k})\sin\alpha_{t_i}\sin\alpha'_{t_k}](G_{n+1} - G_{n-1})\rho_{t_i}\rho'_{t_k}, \qquad (2.33) \\
\\
\left(Z_n^{\phi\phi}\right)_{ik} &= \pi\rho_{t_i} - \frac{1}{2}\{-2G_n\rho'_{t_k}\cos\alpha_{t_i} + [\rho_{t_i}\cos\alpha_{t_i} - (z_{t_i} - z'_{t_k})\sin\alpha_{t_i}] \\
&\quad \cdot(G_{n+1} + G_{n-1})\}\rho_{t_i}\rho'_{t_k},
\end{aligned}$$

and

$$
\begin{aligned}
\left(V_n^t\right)_i &= 2\pi H'^{t}_{inc,n}(t_i)\rho_{t_i}, \\
\left(V_n^\phi\right)_i &= 2\pi H'^{\phi}_{inc,n}(t_i)\rho_{t_i}.
\end{aligned}
\tag{2.34}
$$

where

$$
G_n = \begin{cases} \displaystyle\int_0^\pi \frac{\cos\, n\phi'}{[\rho_{t_i}^2 + \rho_{t_k}'^2 - 2\rho_{t_i}\rho_{t_k}' \cos\phi' + (z_{t_i} - z_{t_k}')]^{3/2}}\, d\phi' & i \neq k, \\ \\ \displaystyle\int_{0^+}^\pi \frac{\cos\, n\phi'}{[2\rho_{t_i}^2 - 2\rho_{t_i}^2 \cos\phi']^{3/2}}\, d\phi' \qquad i = k,\ \phi' \in (0, \pi]. & \end{cases}
\tag{2.35}
$$

The subscripts t_i and t_k indicates the values of ρ, α and z at $t = t_i$ and ρ', α' and z' at $t = t_k$, respectively. The integration G_n is performed numerically using a suitable integration algorithm (see Section 3.1.2).

2.3.2 Impedance Matrix Elements with Impulse Weighting Functions and Pulse Basis Functions

Pulse basis functions represent a more realistic distribution of current. It assumes that the induced currents are distributed evenly along a segment. So, we choose

$$
f_k(t) = \begin{cases} 1 & (k-1) \leq t \leq k, \\ 0 & elsewhere. \end{cases}
\tag{2.36}
$$

Under the assumption that ρ_{t_k}, α_{t_k} and z_{t_k} remain constant and equal to their values at the midpoint of each segment, (2.33) holds true for this case too, but the values of G_n will be modified. For pulse basis functions

$$
G_n = \begin{cases} \displaystyle\int_0^\pi f(\phi')d\phi' & i \neq k, \\ \\ \displaystyle\int_{0^+}^\pi f(\phi')d\phi' & i = k,\ \phi' \in (0, \pi]. \end{cases}
\tag{2.37}
$$

where $f(\phi') = \displaystyle\int_{k-1}^{k} \frac{\cos\ n\phi'}{R_{t_i}^3}\, dt'$ and $R_{t_i} = [\rho_{t_i}^2 + \rho'^2 - 2\rho_{t_i}\rho' \cos\phi' + (z_{t_i} - z')]^{\frac{1}{2}}$. By assuming t' to be a straight line between $k-1$ and k, we obtain

$$f(\phi') = \int_{t_k-0.5}^{t_k+0.5} \frac{dt'}{(t'^2 + d^2)^{3/2}}, \tag{2.38}$$

where

$$\begin{aligned}
t_k &= |(\rho_{t_i} \cos\phi' - \rho'_{t_k}) \sin\alpha_{t_k} + (z_{t_i} - z'_{t_k}) \cos\alpha_{t_k}|, && (2.39)\\
d &= \sqrt{R_{ik}^2 - t_k^2} \qquad \text{and} && (2.40)\\
R_{ik} &= [\rho_{t_i}^2 + \rho'^2_{t_k} - 2\rho_{t_i}\rho'_{t_k} \cos\phi' + (z_{t_i} - z'_{t_k})]^{\frac{1}{2}}. && (2.41)
\end{aligned}$$

Evaluation of the integration in (2.38) yields

$$f(\phi') = \frac{t_k + 0.5}{d^2\sqrt{(t_k + 0.5)^2 + d^2}} - \frac{t_k - 0.5}{d^2\sqrt{(t_k - 0.5)^2 + d^2}}. \tag{2.42}$$

Chapter 3

Spheroids in Axisymmetric Fields

Let us now consider a perfect conducting spheroid either prolate or oblate, placed in an axisymmetric field. The semi-major and the semi-minor axis in case of a prolate spheroid are a_0 and b_0, respectively, while in case of an oblate spheroid, they are b_0 and a_0, respectively.

A perfect conducting prolate spheroid in a $\hat{z}$ directed uniform field is shown in Fig. 3.1. The geometry of the spheroid is expressed in prolate spheroidal coordinates η^*,ξ^*,ϕ^* ($-1 \leq \eta^* \leq +1, 1 \leq \xi^* \leq \infty$, and $0 \leq \phi^* \leq 2\pi$) defined with respect to the center of the spheroid. The relationship between the length of the meridian (see Section 2.3.1) and the spheroid dimensions is

$$N = C_0 b_0 \sqrt{k_{ab}^2 - 1}, \tag{3.1}$$

where the axial ratio $k_{ab} = a_0/b_0$ and

$$C_0 = \int_{-1}^{1} \left[\frac{\xi_0^{*2} - \eta^{*2}}{1 - \eta^{*2}} \right]^{\frac{1}{2}} d\eta^*. \tag{3.2}$$

Here, ξ_0^* is the prolate spheroid surface equation, with $\xi_0^* = k_{ab}\sqrt{k_{ab}^2 - 1}$. The prolate spheroidal coordinates are related to the rectangular cartesian coordinates (x^*,y^*,z^*)

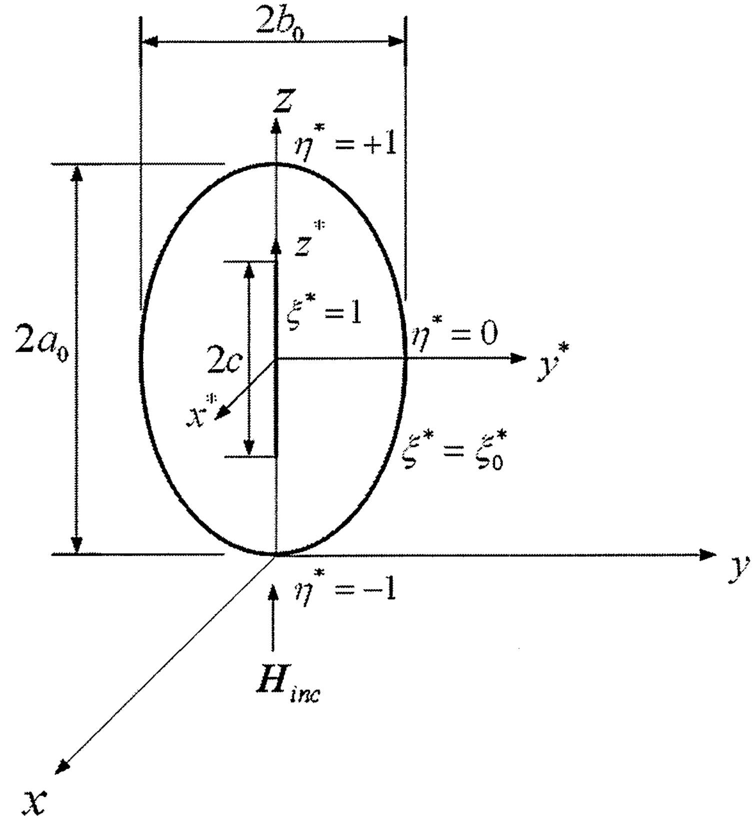

Figure 3.1: Perfect conducting prolate spheroid in a $\hat{\mathbf{z}}$ directed uniform field.

whose origin is at the center of the spheroid by [7]

$$\begin{aligned} x^* &= c[(1-\eta^{*2})(\xi^{*2}-1)]^{1/2}\cos\phi^* \\ y^* &= c[(1-\eta^{*2})(\xi^{*2}-1)]^{1/2}\sin\phi^* \\ z^* &= c\eta^*\xi^*. \end{aligned} \tag{3.3}$$

The corresponding scale factors h_{η^*},h_{ξ^*} and h_{ϕ^*} are [7]

$$
\begin{aligned}
h_{\eta^*} &= c\left[\frac{\xi^{*2}-\eta^{*2}}{1-\eta^{*2}}\right]^{1/2} \\
h_{\xi^*} &= c\left[\frac{\xi^{*2}-\eta^{*2}}{\xi^{*2}-1}\right]^{1/2} \\
h_{z^*} &= c[(1-\eta^{*2})(\xi^{*2}-1)]^{1/2},
\end{aligned}
\tag{3.4}
$$

where c is the semi-focal length of the prolate spheroid, $c = \sqrt{a_0^2 - b_0^2}$.

To compute the impedance matrix, the required geometric parameters of the spheroid ρ and z are calculated using (3.3) with $\xi^* = \xi_0^*$ and $\phi^* = 0$ (the observations are made on the meridian at $\phi = 0$, $\rho = x^*$ and $z = z^* + a_0$). The η^* coordinates at the middle of each segment is found from

$$\int_{-1}^{\eta_k^*} h_{\eta^*} d\eta^* = k - 0.5, \qquad\qquad k = 1, 2, ...N. \tag{3.5}$$

Since the generating curve C for the prolate spheroid is an ellipse given by

$$C \equiv x^2/b_0^2 + (z - a_0)^2/a_0^2 = 1. \tag{3.6}$$

from (2.25) we have

$$\alpha = \tan^{-1}\left(\frac{a_0 - z}{x}\right). \tag{3.7}$$

We present numerical results for two cases of axisymmetric fields: a $\hat{\mathbf{z}}$ directed uniform magnetic field and the magnetic field produced by a coaxial circular current-carrying turn. In Section 3.2.4, a sphere in the presence of a circular turns with its axis along the z-axis is presented as a special case.

3.1 Spheroids in a Uniform Magnetic Field Directed Along the Axis of Rotation

A uniform magnetic field incident along the axis of rotation is the most simplest of cases. Due to the axisymmetry in the system, the magnetic vector potential has a ϕ component only. Hence, the external magnetic field on the conductor surface is along the meridian derection.

3.1.1 Computation of the Inducing Field Matrix Entries

As shown in Fig. 3.1, we select the z-axis of our coordinate system along the body's axis of rotation. Then the inducing magnetic field can be written as $\boldsymbol{H}_{inc}(\boldsymbol{r}) = H_{inc}\hat{\boldsymbol{z}}$. To compute the inducing field matrix, the external field is expressed in terms of the local vectors defined in (2.24) as

$$\boldsymbol{H}_{inc}(\mathrm{r}) = H_{inc}(\hat{\boldsymbol{t}}\cos\alpha - \hat{\boldsymbol{n}}\sin\alpha). \tag{3.8}$$

Since this field is independent of ϕ, Fourier series expansion in azimuthal angle (2.17) contains only the component corresponding to $m = 0$. Thus (2.34) yields

$$\begin{aligned} \left(V_0^t\right)_i &= 0 \qquad \text{and} \\ \left(V_0^\phi\right)_i &= -2\pi H_{inc}\rho_{t_i}\cos\alpha_{t_i}. \end{aligned} \tag{3.9}$$

After the impedance and inducing field matrices are computed, (2.19) is used to determine the coefficients I_{0k}^t and I_{0k}^ϕ. The surface current density is calculated using (2.16) and the resultant magnetic field intensity on the surface of the body is given by

$$\boldsymbol{H}(\mathrm{r}) = -\hat{\boldsymbol{n}} \times \hat{\boldsymbol{J}}_s(\mathrm{r}). \tag{3.10}$$

3.1.2 Results for Prolate Spheroids

We consider a perfect conducting prolate spheroid in a uniform magnetic field directed along the major axis. The meridian is divided into N number of segments and we use Dirac delta functions as basis functions.

Using impulse basis functions

To evaluate the integration in (2.35), we use adaptive Lobatto quadrature algorithm with an absolute error tolerance of 10^{-6}.

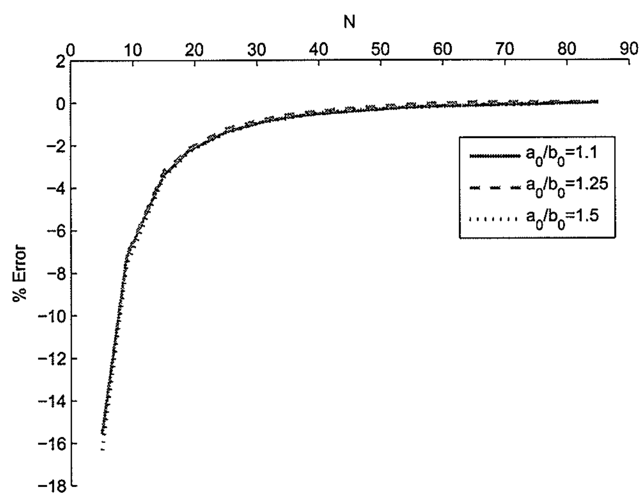

Figure 3.2: Percentage error of the normalized tangential magnetic field at $\eta^* = 0$ versus the number of meridian segments, for various a_0/b_0.

Figure 3.2 shows the effect of the number of meridian segments on the convergence of the normalized tangential magnetic field at $\eta^* = 0$. The error is calculated with respect to the normalized tangential magnetic field at the same location with 85 impulse basis functions. Results are presented for prolate spheroids with three different axial ratios. Figure 3.2 shows that by using more than 31 meridian segments, a significant accuracy (absolute percentage error less than 1%) at the middle of the meridian can be achieved.

The normalized tangential magnetic fields generated with 31 and 85 meridian segments are compared in Table 3.1. The maximum deviation in the solution with $N = 31$ compared to the one with $N = 85$ is 2.63%, observed for the prolate spheroid with $a_0/b_0 = 1.5$ at $|\eta^*| = 0.9$.

Table 3.1: Normalized magnetic field generated with 31 and 85 meridian segments, at several locations along the meridian of a prolate spheroid with different axial ratios.

N	$\|\eta^*\|$	H/H_{inc}		
		$a_0/b_0 = 1.1$	$a_0/b_0 = 1.25$	$a_0/b_0 = 1.5$
31	0	1.446	1.395	1.337
	0.6	1.197	1.193	1.200
	0.9	0..672	0.715	0.776
85	0	1.459	1.406	1.349
	0.6	1.205	1.209	1.209
	0.9	0.684	0.730	0.797

In Fig. 3.3, the normalized tangential magnetic field generated using 31 meridian segments and the exact solution given in (A.18), are shown for spheroids with $a_0/b_0 = 1.1, 1.25$ and 1.5. Details of the derivation of the exact solution are given in Appendix A. This comparison is possible because $\hat{\boldsymbol{\eta}}^*$ is along the meridian and therefore is same as $\hat{\boldsymbol{t}}$.

The percentage error of the generated results with respect to the exact solution are plotted in Fig. 3.4. The accuracy in the results is lower for points closer to the poles. Another interesting observation is that the deviation from the exact solution is getting higher as the axial ratio increases from unity.

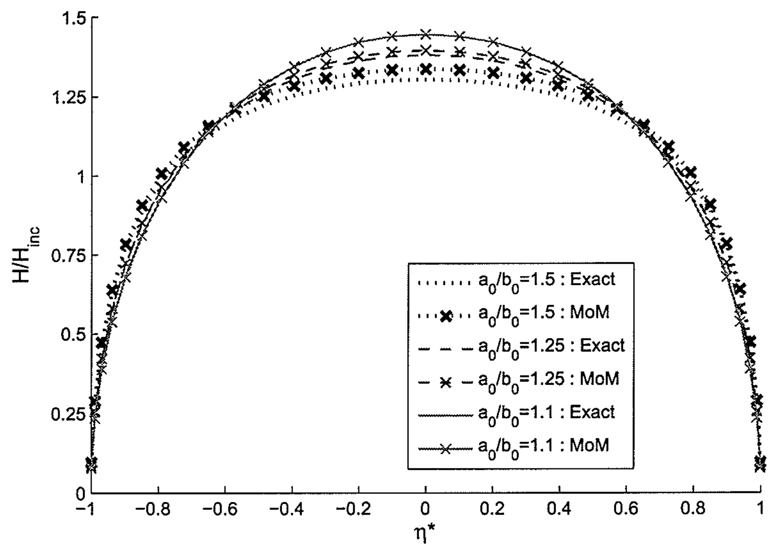

Figure 3.3: Normalized magnetic fields generated using the MoM and the exact solution for a prolate spheroid with three different axial ratios, impulse basis functions and N=31, excited by an axially directed uniform field.

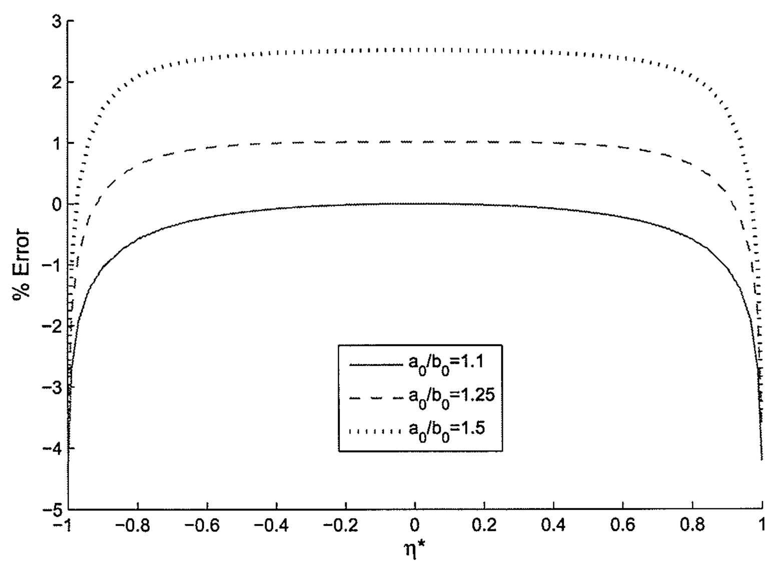

Figure 3.4: Percentage error with respect to the exact solution of the normalized magnetic field along the meridian for a prolate spheroid with three different axial ratios, impulse basis functions and N=31, excited by an axially directed uniform field.

Using pulse basis functions

Using fewer meridian segments when calculating the tangential magnetic field intensity with impulse basis functions introduces errors, because the surface current density is assumed to be concentrated at the center of each segment. Pulse basis functions give a better approximation to the distribution of surface current density.

To compute the impedance matrix with pulse basis functions, G_n is calculated from (2.37). As in the case with impulse basis functions, the integral is evaluated using the adaptive Lobatto quadrature algorithm with an absolute error tolerance of 10^{-6}.

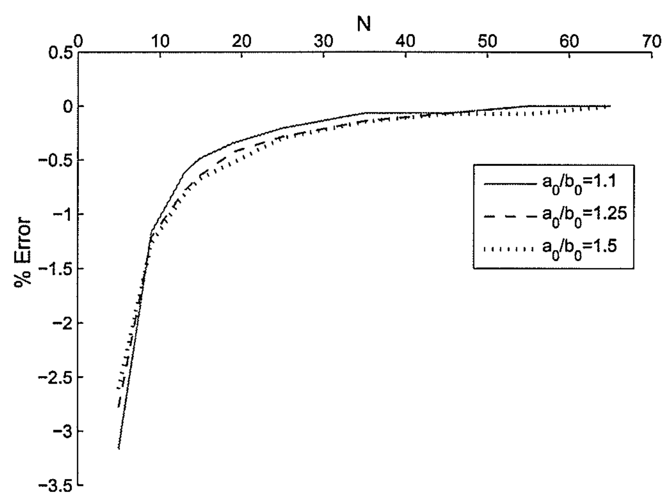

Figure 3.5: Percentage error of the normalized magnetic field at $\eta^* = 0$ versus the number of meridian segments, for various a_0/b_0.

Figure 3.5 shows the variation of the percentage error with the number of meridian segments, for prolate spheroids with three different axial ratios. The percentage error of the normalized tangential magnetic field at $\eta^* = 0$ is evaluated with respect to the value computed with $N = 65$. To have an absolute percentage error less than 1%, the meridian needs to be divided into more than 12 segments.

The normalized tangential magnetic field intensities generated with 13 and 65 segments are compared in Table 3.2. The maximum deviation in the solution with $N = 13$ as compared to the one with $N = 65$ is 4.36%, observed for the spheroid with $a_0/b_0 = 1.25$ at $|\eta^*| = 0.9$.

Table 3.2: Normalized magnetic field intensity generated with 13 and 65 meridian segments, at several locations along the meridian of a prolate spheroid with different axial ratios.

N	$\lvert\eta^*\rvert$	H/H_{inc}		
		$a_0/b_0 = 1.1$	$a_0/b_0 = 1.25$	$a_0/b_0 = 1.5$
	0	1.445	1.391	1.331
13	0.6	1.185	1.188	1.189
	0.9	0..659	0.702	0.766
	0	1.454	1.402	1.342
65	0.6	1.203	1.206	1.205
	0.9	0.687	0.734	0.800

The normalized tangential magnetic field intensity at $\eta^* = 0$ computed with 13 segments, is compared with that from the exact solution. For prolate spheroids with axial ratios of 1.1, 1.25 and 1.5, the variation of the percentage error along the meridian is shown in Fig. 3.6. The employment of pulse basis functions results in a lesser deviation from the exact solution as compared to the deviation when using impulse basis functions, especially closer to the poles.

The computation times of the magnetic field on the surface of prolate spheroids with the three axial ratios tested, with pulse basis functions and 13 segments, and with impulse basis functions and 31 segments are given in Table 3.3. Computation was performed with a notebook computer with Intel Centrino® Duo processor working at 2GHz. Pulse basis functions yield a faster convergence when compared to the impulse basis functions, due to the smaller number of segments required. Because of its higher efficiency as compared to the impulse basis functions, here after we use pulse basis functions to obtain the numerical results.

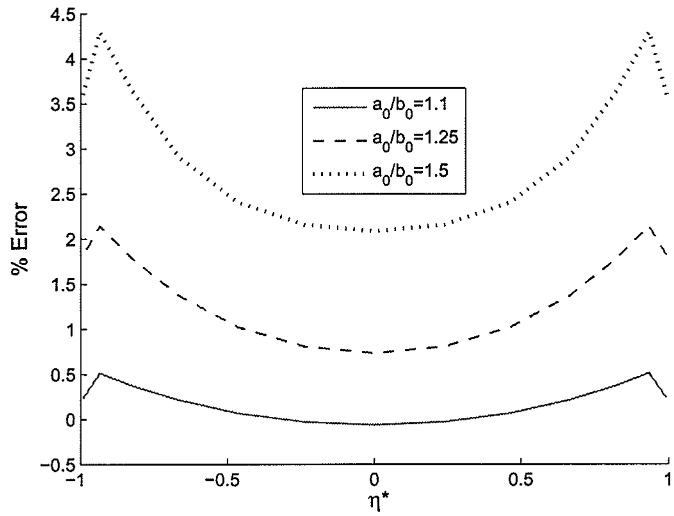

Figure 3.6: Percentage error with respect to the exact solution of the normalized magnetic field along the meridian for a prolate spheroid with three different axial ratios, pulse basis functions and N=13, excited by an axially directed uniform field.

Table 3.3: Comparison of the CPU time to obtain a percentage deviation of 1%, with the two types of basis functions used .

N	CPU time (s)		
	$a_0/b_0 = 1.1$	$a_0/b_0 = 1.25$	$a_0/b_0 = 1.5$
13;Pulse	2.15	2.18	2.20
31;Impulse	4.92	4.86	4.81

3.1.3 Results for Oblate Spheroids

Consider now the case of a perfect conducting oblate spheroid in a uniform field directed along the minor axis. By using the transformations $\xi^* \rightarrow j\xi^*$, $\xi_0^* \rightarrow j\xi_0^*$ and $c \rightarrow -jc$ [7], the corresponding matrix elements for the oblate spheroid are obtained from those for the prolate spheroid.

For oblate spheroids with axial ratios of 0.9, 0.8 and 0.7 in an axially directed uniform magnetic field, the numerical results for the normalized tangential magnetic field intensity at $\eta^* = 0$ generated with different numbers of meridian segments are compared with those obtained with 45 meridian segments. Figure 3.7 shows that, by dividing the meridian into at least 11 segments, an absolute percentage error of less than 1% can be achieved.

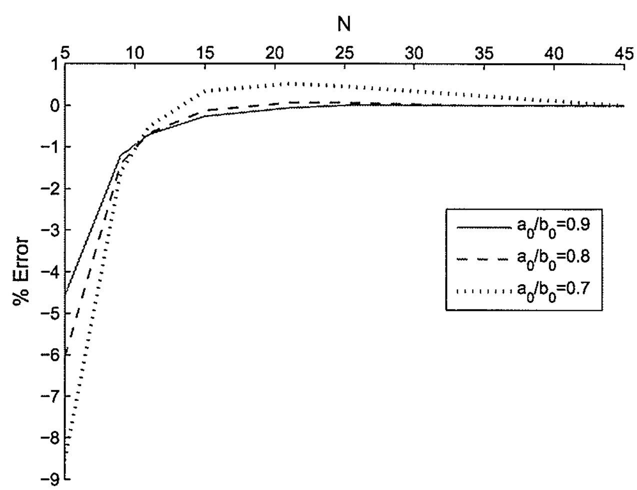

Figure 3.7: Percentage error of the normalized tangential magnetic field at $\eta^* = 0$ versus the number of meridian segments, for various a_0/b_0.

The generated normalized tangential magnetic field intensity with 11 segments and the exact solution in (A.19) are given in Fig. 3.8 and they are compared in Fig. 3.9 via the percentage error with respect to the exact solution.

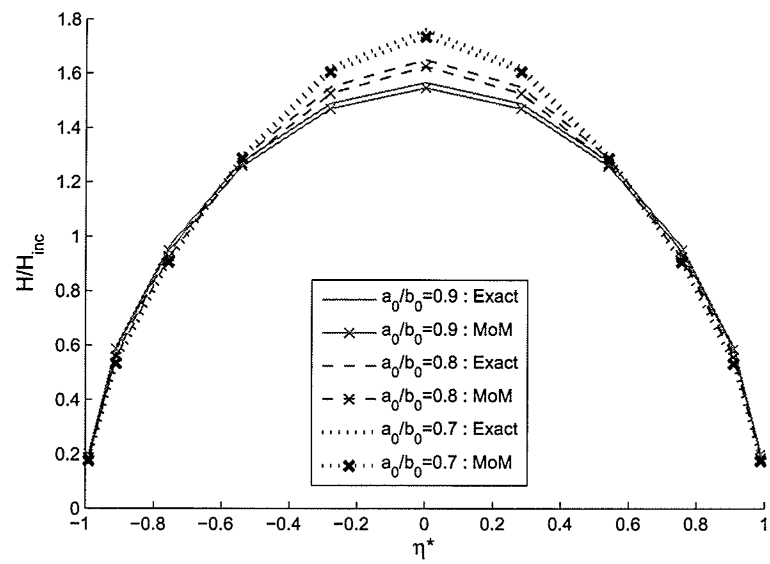

Figure 3.8: Normalized magnetic fields generated using the MoM and the exact solution for an oblate spheroid with three different axial ratios and N=11, excited by an axially directed uniform field.

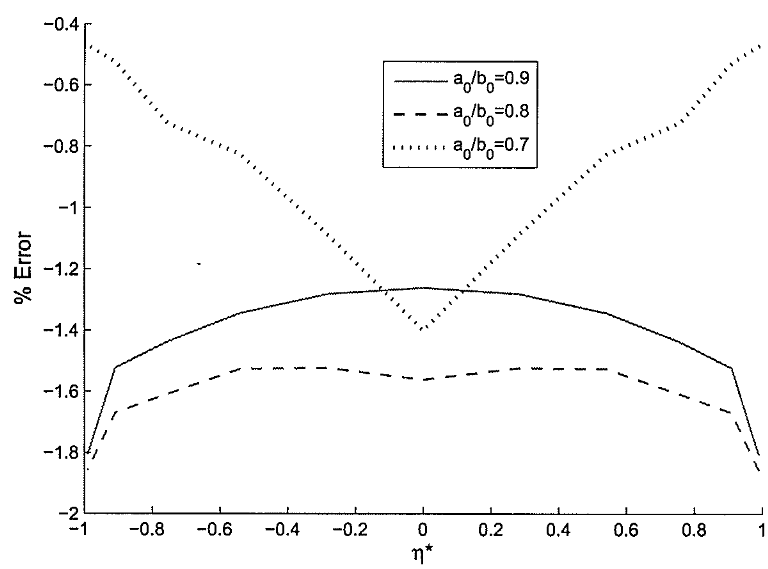

Figure 3.9: Percentage error with respect to the exact solution of the normalized magnetic field along the meridian for an oblate spheroid with three different axial ratios and N=11, excited by an axially directed uniform field.

3.2 Spheroids in the Presence of Coaxial Circular Current-Carrying Turns

Consider a perfect conducting prolate spheroid in the presence of a circular current-carrying turn as shown in Fig. 3.10. Since the geometry of the prolate spheroid remains the same, the impedance matrix calculated in the pervious section is not affected.

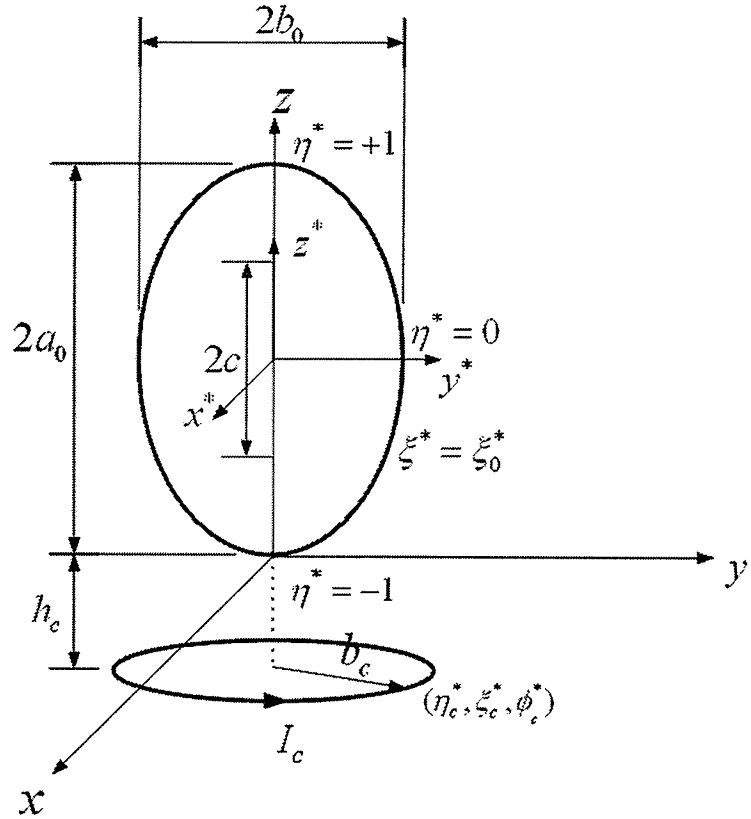

Figure 3.10: A perfect conducting prolate spheroid in the presence of a coaxial circular current-carrying turn.

3.2.1 Computation of the Inducing Field Matrix

We first calculate the magnetic field intensity produced by the circular current-carrying turn at the middle of the meridian segments. The magnetic field intensity $\boldsymbol{H}_{inc}$ produced by a circular current-carrying turn is given in [12],

$$\boldsymbol{H}_{inc} = H^{\rho}_{inc}\hat{\boldsymbol{\rho}} + H^{z}_{inc}\hat{\boldsymbol{z}}, \tag{3.11}$$

where

$$\begin{aligned} H^{\rho}_{inc} &= \frac{I_c(z+h_c)}{2\pi\rho\sqrt{(b_c+\rho)^2+(z+h_c)^2}}\left[-K+\frac{b_c^2+\rho^2+(z+h_c)^2}{(b_c-\rho)^2+(z+h_c)^2}E\right] && (3.12)\\ H^{z}_{inc} &= \frac{I_c}{2\pi\sqrt{(b_c+\rho)^2+(z+h_c)^2}}\left[K+\frac{b_c^2-\rho^2-(z+h_c)^2}{(b_c-\rho)^2+(z+h_c)^2}E\right]. && (3.13)\end{aligned}$$

Here, K and E are complete elliptic integrals of the first and second kind, respectively, with modulus $\sqrt{4b_c\rho/\left[(b_c+\rho)^2+(z+h_c)^2\right]}$ (see notation in Fig. 3.10). Using the cylindrical to cartesian coordinate transform and the relationships given in (2.24), the right hand side in (2.6) is determined in the form

$$\boldsymbol{H}'_{inc} = -(H^{\rho}_{inc}\sin\alpha + H^{z}_{inc}\cos\alpha)\hat{\boldsymbol{\phi}}. \tag{3.14}$$

Independence of ϕ in $\boldsymbol{H}'_{inc}$ results in its Fourier expansion to have only the $n = 0$ component. Therefore, from (2.34), the inducing field matrix elements are

$$\begin{aligned} \left(V_0^t\right)_i &= 0 \qquad \text{and} \\ \left(V_0^{\phi}\right)_i &= -2\pi[H^{\rho}_{inc}(t_i)\sin\alpha_{t_i} + H^{z}_{inc}(t_i)\cos\alpha_{t_i}]\rho_{t_i}. && (3.15)\end{aligned}$$

The inducing field matrix for an axisymmetric system with multiple coaxial turns can be computed simply by using the superposition.

3.2.2 Results for Prolate Spheroids

To evaluate the complete elliptic integrals in (3.12) and (3.13), we use the subroutine given in Matlab which is based on the method of arithmetic geometric mean [13]. The magnetic field intensity on the surface of the prolate spheroid is normalized with respect to I_c/b_0 and the ratio h_c/b_c is kept at unity, in all cases.

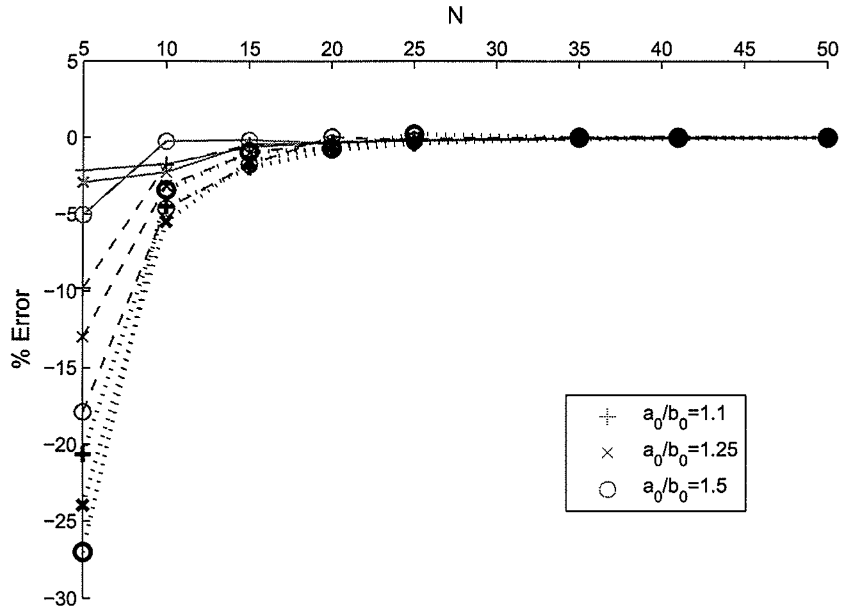

Figure 3.11: Percentage error of the maximum value of the normalized tangential magnetic field versus the number of meridian segments , for various a_0/b_0 and b_0/b_c: $b_0/b_c = 0.25$ ———; $b_0/b_c = 0.5$ - - - -; $b_0/b_c = 0.75$ $\cdots\cdot$.

Figure 3.11 shows the effect of the number of meridian segments on the convergence of the solution for the maximum value of the normalized magnetic field intensity on the surface of the prolate spheroid. The percentage error of the maximum tangential magnetic field is calculated with respect to the result obtained with 50 segments and is plotted against the number of meridian segments for prolate spheroids with various axial ratios and $b_0/b_c = 0.25,\ 0.5,$ and 0.75. Using more than 25 segments yields an absolute percentage error less than 0.5% for all the cases.

The magnetic field problem for a perfect conducting prolate spheroid in the presence of a coaxial current-carrying circular turn can be solved analytically. Details of the derivation are given in Appendix A. We compare the results obtained from the method of moments with the exact solution given in (A.13). Analytical computation of tangential magnetic field requires the calculation of associated Legendre functions with various arguments. Numerical values of P_p^1 and Q_p^1 for arguments smaller than 1 are obtained using the recurrence formulas [13]. The algorithm in [14] is used to calculate P_p^1 for arguments greater than one, while Q_p^1 for such arguments is calculated with the algorithm in [15].

Figures 3.12, 3.14 and 3.16 show the normalized tangential magnetic field intensity calculated using 25 meridian segments and the exact solution for prolate spheroids with axial ratios of 1.1, 1.25 and 1.5, excited by a coaxial circular current-carrying turn with $b_0/b_c = 0.25,\ 0.5$ and 0.75, respectively. The series in the exact solution is truncated at 25 terms [6].

In Fig.s 3.13, 3.15 and 3.17 we compare the normalized tangential magnetic field intensity for all the cases, computed from the two methods. The percentage error is calculated with respect to the exact solution. Although a large percentage error is present closer to the pole opposite to the turn, in all the cases tested, it is less than 5% when $\eta^* \in [-1, 0.5]$.

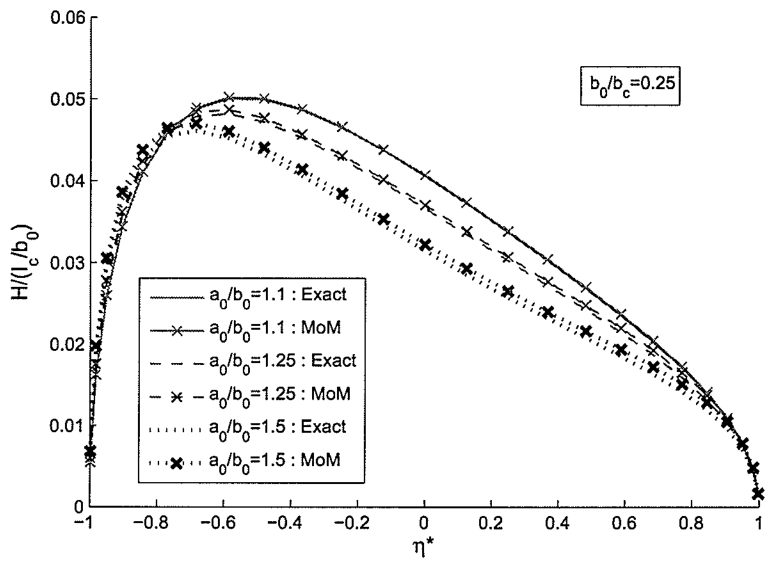

Figure 3.12: Normalized magnetic field generated using the MoM and the exact solution for a prolate spheroid with different axial ratios excited by a coaxial turn with $h_c/b_c = 1$, $b_0/b_c = 0.25$ and $N = 25$.

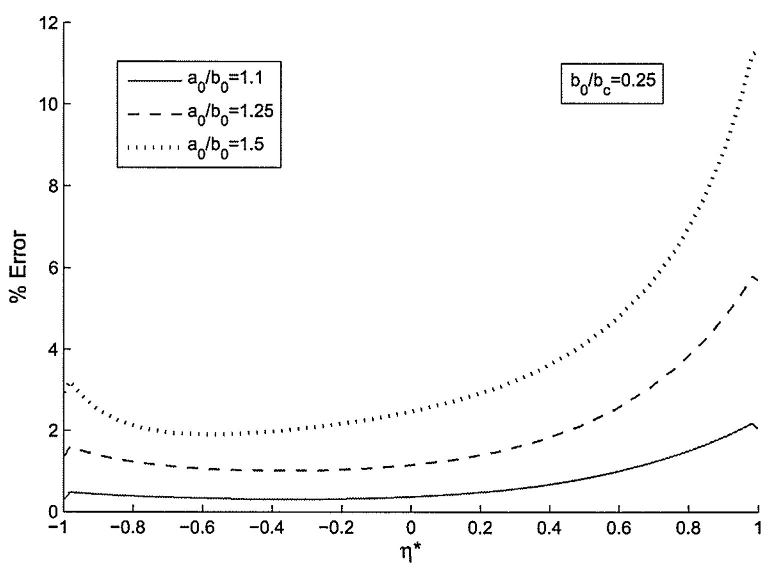

Figure 3.13: Percentage error with respect to the exact solution of the normalized magnetic field along the meridian for a prolate spheroid with different axial ratios exited by a coaxial turn with $h_c/b_c = 1$, $b_0/b_c = 0.25$ and $N = 25$.

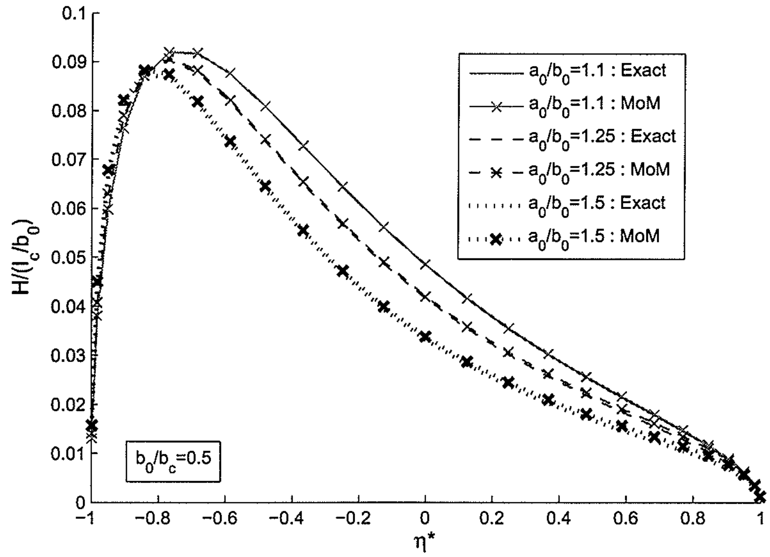

Figure 3.14: Normalized magnetic field generated using the MoM and the exact solution for a prolate spheroid with different axial ratios excited by a coaxial turn with $h_c/b_c = 1$, $b_0/b_c = 0.5$ and $N = 25$.

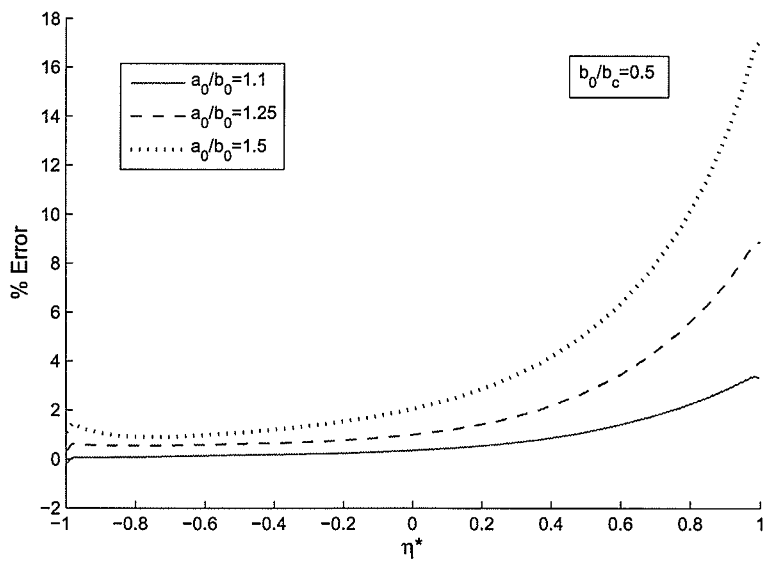

Figure 3.15: Percentage error with respect to the exact solution of the normalized magnetic field along the meridian for a prolate spheroid with different axial ratios exited by a coaxial turn with $h_c/b_c = 1$, $b_0/b_c = 0.5$ and $N = 25$.

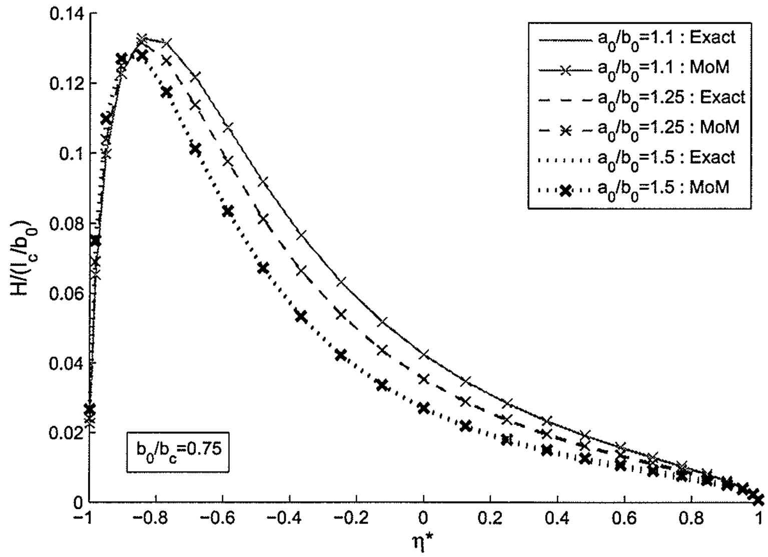

Figure 3.16: Normalized magnetic field generated using the MoM and the exact solution for a prolate spheroid with different axial ratios excited by a coaxial turn with $h_c/b_c = 1$, $b_0/b_c = 0.75$ and $N = 25$.

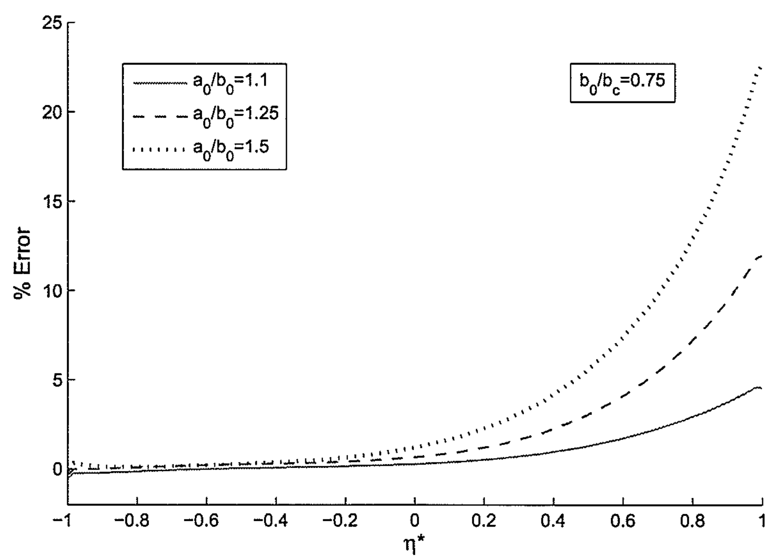

Figure 3.17: Percentage error with respect to the exact solution of the normalized magnetic field along the meridian for a prolate spheroid with different axial ratios exited by a coaxial turn with $h_c/b_c = 1$, $b_0/b_c = 0.75$ and $N = 25$.

3.2.3 Results for Oblate Spheroids

Applying the transformations in Section 3.1.3 to obtain the results for oblate spheroids from those for prolate spheroids introduces associated Legendre functions of second kind with imaginary arguments in the calculation of the exact solution for the tangential magnetic field in the presence of a coaxial current-carrying circular turn. The algorithm given in [15] is used to compute Q_p^1 with imaginary arguments. The exact solution in (A.14) is truncated to 25 terms [6].

Results for the normalized tangential magnetic field generated with $N = 25$ meridian segments are presented for oblate spheroids with axial ratios of 0.9 and 0.75. The tangential magnetic field is normalized with respect to I_c/a_0. The suitable number of basis functions was obtained by calculating the percentage error of the maximum value of the tangential magnetic field for different N's with respect to the value obtained with $N = 50$. It was found that when the number of basis functions is grater than or equal to 25, the relative error is less than 0.5%. The results presented have been obtained by keeping the ratio h_c/b_c at unity while changing the ratio a_0/b_c.

The normalized tangential magnetic field intensity computed by using the method of moments and its exact solution are plotted in Fig. 3.18; a comparison between the two in terms of the percentage error is shown in Fig. 3.19. Results are given for $a_0/b_c = 0.25$, $a_0/b_c = 0.5$, and $a_0/b_c = 0.25$. A significant accuracy (absolute percentage error less than 2%) compared to the exact solution can be obtained for $\eta^* \in [-1.3, 0.4]$.

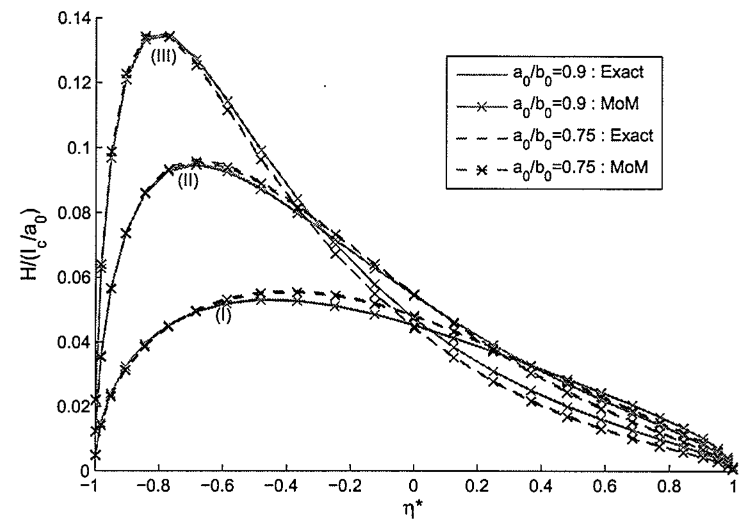

Figure 3.18: Normalized magnetic field obtained by using the MoM and the exact solution for an oblate spheroid with different axial ratios and $N = 25$, excited by a coaxial turn with $h_c/b_c = 1$ and a_0/b_c: (I) $a_0/b_c = 0.25$; (II) $a_0/b_c = 0.5$; (III) $a_0/b_c = 0.75$.

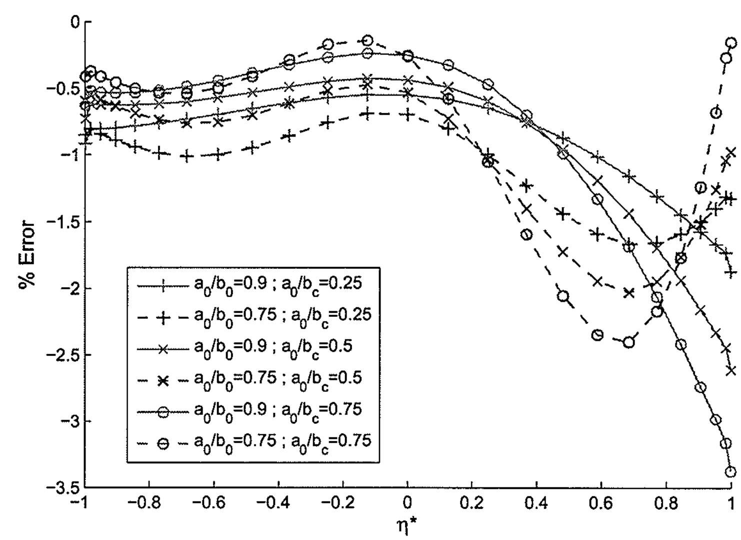

Figure 3.19: Percentage error with respect to the exact solution of the normalized magnetic field along the meridian for an oblate spheroid with different axial ratios and $N = 25$, exited by a coaxial turn with $h_c/b_c = 1$ and different values of a_0/b_c.

3.2.4 The Special Case of Spheres

A sphere is a spheroid with an axial ratio $k_{ab} = 1$. The results obtained for the prolate spheroid can be reduced to those for a sphere by using the transformations [7]

$$\begin{gathered} c \to 0\,; \qquad \xi_0^*, \xi_c^*, \xi^* \to \infty\,; \qquad \eta_c^* \to \cos\theta_c^*,\ \eta^* \to \cos\theta^*\,; \\ c\xi_0^* \to a_s,\ c\xi_c^* \to r_c^*,\ c\xi^* \to r^*. \end{gathered} \tag{3.16}$$

Here, θ^* is the meridian angle defined with respect to the center of the sphere. As in the previous cases, the subscript c denotes the parameters corresponding to the current-carrying turn; a_s is the radius of the conducting sphere and r_c^* is the radius of the virtual sphere whose center is at the conductor center, containing the circular turn.

By applying the transformations in (3.16) to (3.1), the normalized radius of the sphere is found to be N/π. From (3.3) and (3.5), one obtains in the case of the sphere

$$\begin{aligned} \theta_k^* &= \pi - \frac{k-0.5}{a_s} \\ x_k^* &= a_s \sin\theta_k^* \\ z_k^* &= a_s \cos\theta_k^*. \end{aligned} \tag{3.17}$$

The generating curve is a circle with the center at $(0, 0, a_s)$. Thus, the expression of α in (3.7) is still valid.

The tangential magnetic field is normalized with respect to I_c/a_s. When $N = 25$ meridian segments are used to generate the normalized tangential magnetic field, the relative deviation from the solution with $N = 50$ is less than 0.25% for all the cases presented. Figure 3.20 shows the results generated with $N = 25$ for a sphere excited by a coaxial circular current-carrying turn with $h_c/b_c = 1$ and $a_s/b_c = 0.25,\ 0.5$ and 0.75.

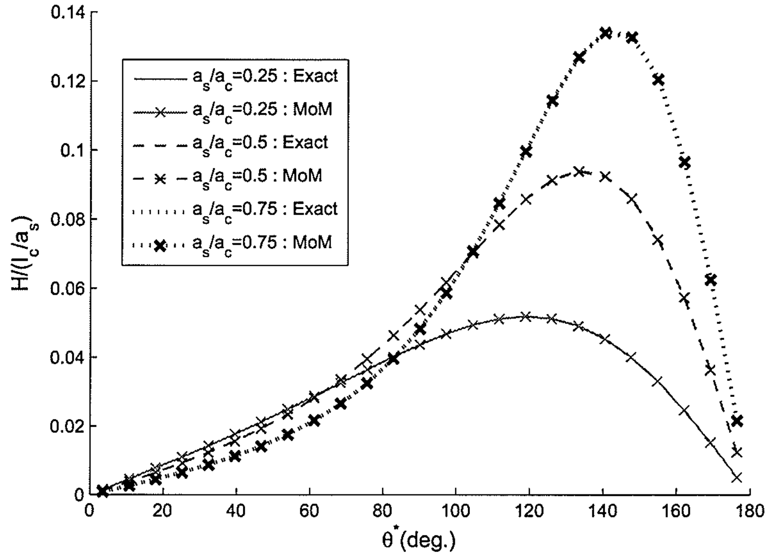

Figure 3.20: Normalized magnetic field generated using the MoM and the exact solution for a perfectly conducting sphere excited by a coaxial turn with $h_c/b_c = 1$ and different a_s/b_c, for $N = 25$.

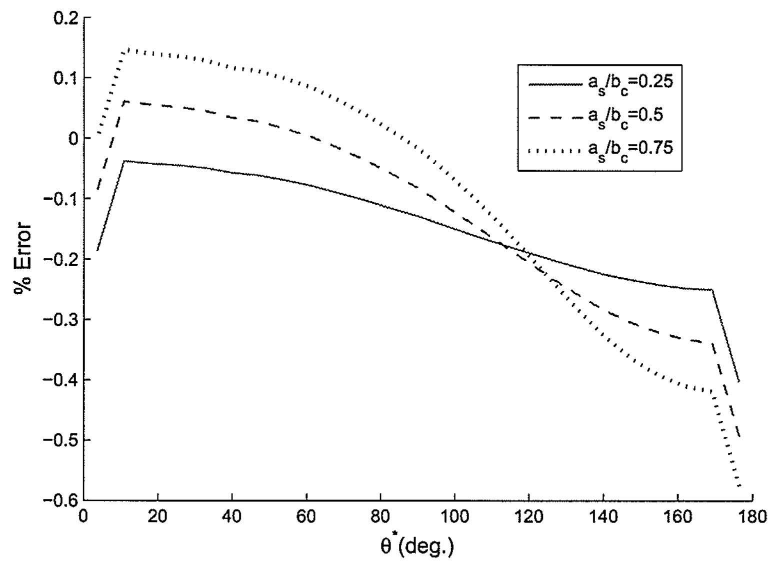

Figure 3.21: Percentage error with respect to the exact solution of the normalized magnetic field along the meridian for a perfectly conducting sphere exited by a coaxial turn with $h_c/b_c = 1$ and different a_0/b_c, for $N = 25$.

In Fig. 3.21, the computed results are compared with those from the exact solution in (A.21). The infinite series for the analytical solution is truncated by retaining only the first 20 terms [16]. The percentage error of the normalized tangential magnetic field is calculated with respect to the exact solution. A much higher accuracy than in the case of spheroids is achieved for the spheres. The error is less than 0.6% everywhere along the meridian.

Chapter 4

Conducting Bodies of Revolution in Arbitrary Fields

In this chapter, the inducing field matrices are calculated for uniform fields directed at an arbitrary angle with respect to the body's axis of symmetry and for the fields produced by circular current-carrying turns whose axes are shifted with respect to the axis of revolution of the body. Numerical results are presented for spheres, prolate and oblate spheroids.

4.1 Uniform Magnetic Field

Let us consider a uniform magnetic field directed at an angle β with respect to the body's axis of revolution. Assume the field to be parallel to the $y-z$ plane, as shown in Fig. 4.1. The cartesian coordinate system is selected such that the $z-$axis is the body's axis of symmetry and the origin is at the bottom of the conductor, as in Fig. 2.2. Then the external inducing magnetic field can be written as

$$\boldsymbol{H}_{inc} = H_{inc}(-\sin\beta\hat{\boldsymbol{y}} + \cos\beta\hat{\boldsymbol{z}}) \tag{4.1}$$

Expressing (4.1) in local unit vectors $\hat{\boldsymbol{t}}$ and $\hat{\boldsymbol{\phi}}$, and expanding its cross product with $\hat{\boldsymbol{n}}$ [the right hand side in (2.6)] in a Fourier series in the azimuthal angle yields the following inducing field matrix elements computed from (2.34)

$$(V_n^t)_i = \begin{cases} 0 & n = 0, \\ -\pi \rho_{t_i} H_{inc} \sin\beta & n = \pm 1, \\ 0 & |n| \geq 2, \end{cases} \tag{4.2}$$

$$(V_n^\phi)_i = \begin{cases} -2\pi \rho_{t_i} H_{inc} \cos\beta \cos\alpha_{t_i} & n = 0, \\ \mp j\pi \rho_{t_i} H_{inc} \sin\beta \sin\alpha_{t_i} & n = \pm 1, \\ 0 & |n| \geq 2. \end{cases} \tag{4.3}$$

Thus, only Fourier modes corresponding to $n = 0$ and $n = \pm 1$ are present in the solution for the surface current density.

4.1.1 Results for Spheres

The impedance matrix for spheres was computed in Section 3.2.4. With (4.2) and (4.3), numerical results for the normalized tangential magnetic field are generated for various angles of β. When 25 meridian segments are used, the relative error with respect to the results obtained with 55 meridian segments is less than 0.2% for all the cases considered.

Figure 4.1 shows the normalized tangential magnetic fields generated using the method of moments and the exact solution given in Appendix B for different values of β. The tangential magnetic field intensity has components along $\hat{\boldsymbol{t}}$ and $\hat{\boldsymbol{\phi}}$ directions, and the resultant tangential magnetic field is normalized with respect to the magnitude of the inducing field. θ^* is the meridian angle coordinate defined with respect to the center of the sphere. For small angles β, the results for the normalized tangential magnetic field are close to the result for the axially incident case especially

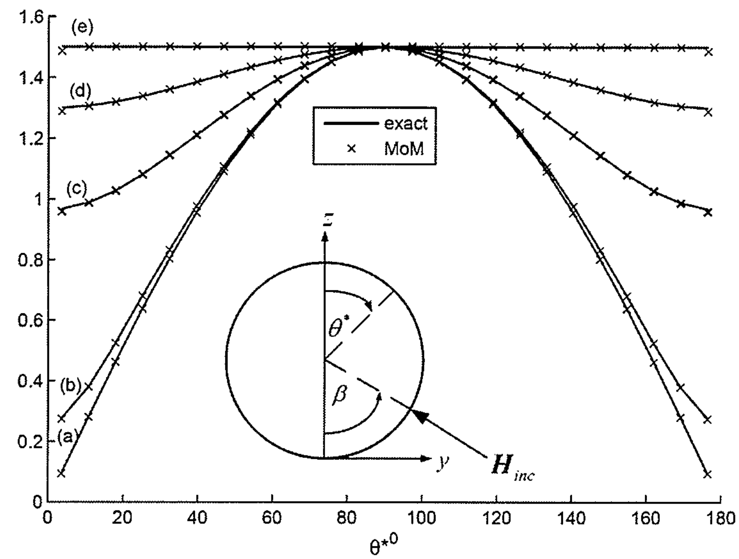

Figure 4.1: Normalized magnetic field at $\phi = 0^0$ generated using the MoM with $N = 25$, and the exact solution for a sphere excited by a uniform magnetic field directed at an angle β with respect to the $z-$axis: (a)$\beta = 0^0$; (b)$\beta = 10^0$; (c)$\beta = 40^0$; (d)$\beta = 60^0$; (e)$\beta = 90^0$.

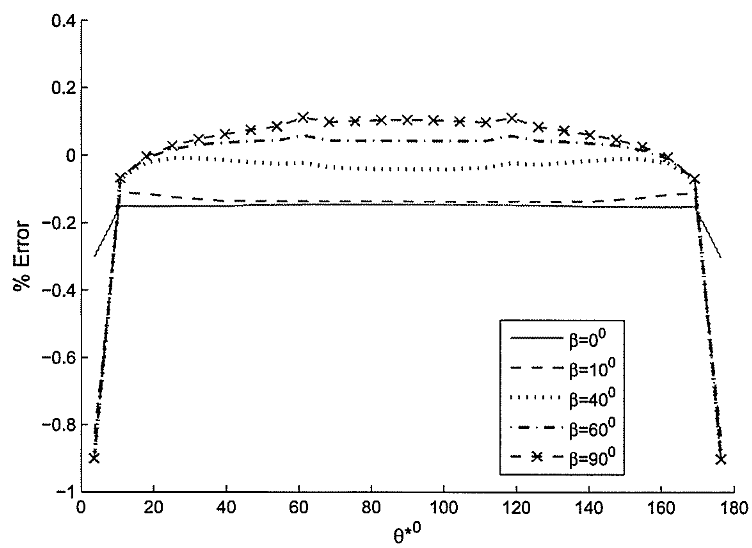

Figure 4.2: Percentage error with respect to the exact solution of the normalized magnetic field at $\phi = 0^0$ for a sphere excited by a uniform magnetic field directed at different angles with respect to the $z-$axis, for $N = 25$.

in the region closer to the middle of the meridian, while a higher deviation from the axially incident field case is observed closer to the poles.

When the inducing field is directed perpendicular to the $z-$ axis, the induced currents at $\phi = 0^0$ are along the meridian and hence the magnetic field on the surface of the sphere is along the $\hat{\boldsymbol{\phi}}$ direction.

The results computed with the method of moments are compared in Fig. 4.2 with the exact solution. A larger deviation from the exact solution is observed closer to the poles and the absolute value of the percentage error of the normalized tangential magnetic field generated with the method of moments with respect to the exact solution is less than 0.2% for $\theta^* \in [10^0, 170^0]$ in all the cases tested.

4.1.2 Results for Spheroids

Numerical results are presented for a prolate spheroid with an axial ratio of 1.25 and for an oblate spheroid with an axial ratio of 0.8 using 25 meridian segments. For all the cases tested, the absolute value of the percentage error with respect to the normalized magnetic field at the middle of the meridian $\phi = 0^0$ is less than 0.3% in the case of the prolate spheroid and less than 0.4% for the oblate spheroid.

Figures 4.3 and 4.4 show the normalized magnetic field intensity along the meridian $\phi = 0^0$ for the prolate spheroid and for the oblate spheroid, respectively, for a uniform inducing field directed at various angles β. The exact solutions corresponding to the axially directed uniform field are also shown for both spheroids. To check the algorithm, results have been generated for a small angles of β ($\leq 10^0$) and compared with the results in the case of an axially directed incident field. As expected, except near the poles, the difference between the two sets of results is relatively small (see the plots for $\beta = 10^0$).

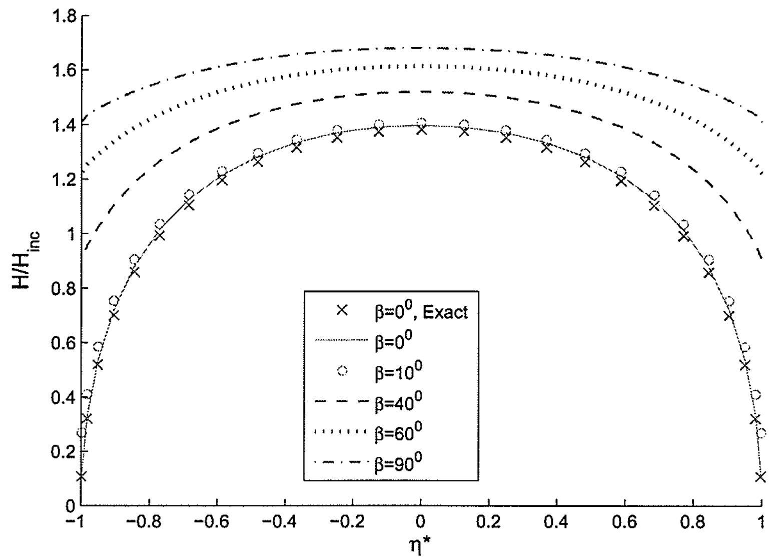

Figure 4.3: Normalized magnetic field at $\phi = 0^0$ for a prolate spheroid with $a_0/b_0 =$ 1.25 in the presence of a uniform inducing field directed at various angles β with respect to the $z-$axis.

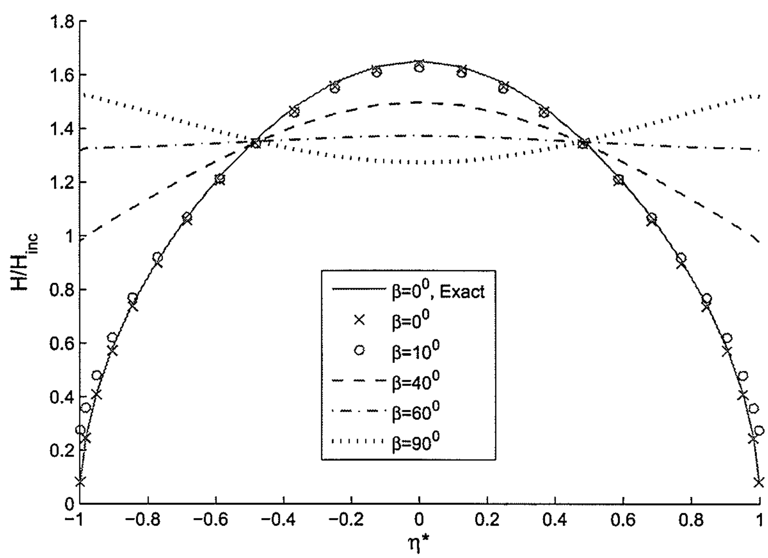

Figure 4.4: Normalized magnetic field at $\phi = 0^0$ for an oblate spheroid with $a_0/b_0 =$ 0.8 in the presence of a uniform inducing field directed at various angles β with respect to the $z-$axis.

4.2 Field from Circular Current-Carrying Turns whose Axes are Shifted with Respect to the Body's Axis of Revolution

Let us shift the axis of the current-carrying turn considered in Section 3.2 by a distance d_c from the axis of revolution of the induced body in $y - z$ plane. Figure 4.5 shows such a turn in the proximity of a prolate spheroid. The components of the inducing magnetic field produced by the circular current-carrying turn at the observation point on the spheroid surface are $\boldsymbol{H}^{\rho_1}$ and $\boldsymbol{H}^{z_1}$.

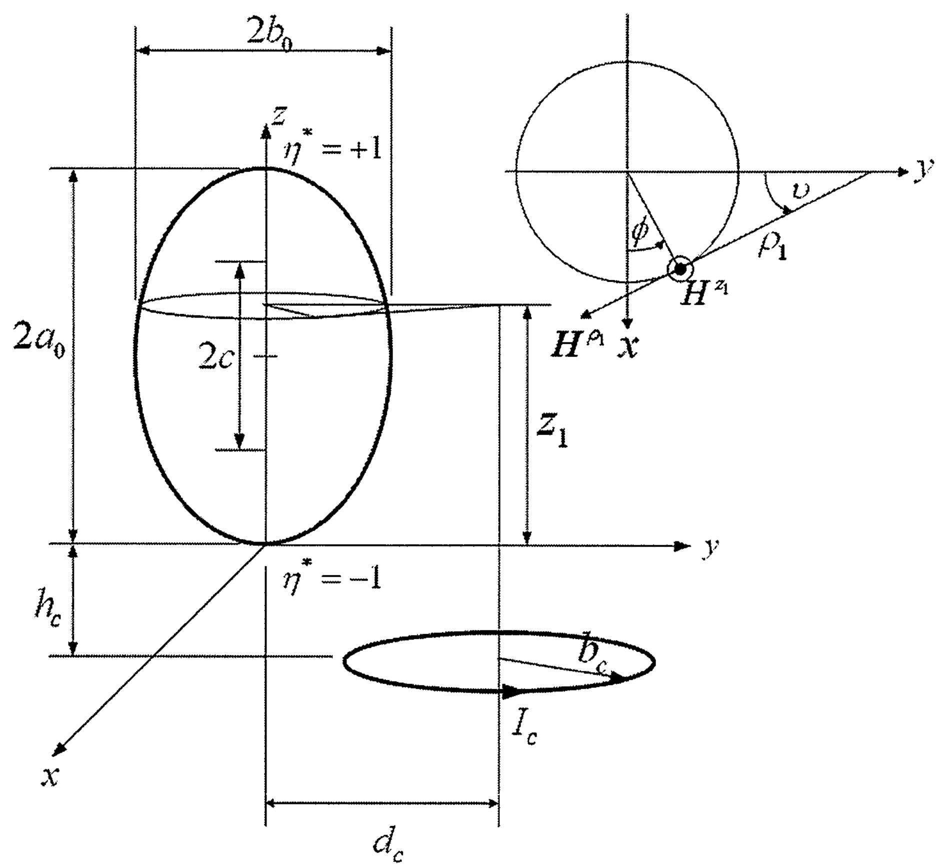

Figure 4.5: Circular turn in the proximity of a conducting spheroid.

4.2.1 Computation of the Inducing Field Matrix

The equations (3.12) and (3.13) are modified to incorporate the shift in the turn axis. In this case, the radial distance from the axis of the turn to the observation point is ρ_1. Therefore, the cylindrical coordinate ρ is replaced with $\rho_1 = \sqrt{\rho^2 + d_c^2 - 2\rho d_c \sin\phi}$. Thus,

$$H_{inc}^{\rho_1} = \frac{I_c(z+h_c)}{2\pi\rho_1\sqrt{(b_c+\rho_1)^2+(z+h_c)^2}}\left[-K + \frac{b_c^2+\rho_1^2+(z+h_c)^2}{(b_c-\rho_1)^2+(z+h_c)^2}E\right] \quad (4.4)$$

$$H_{inc}^{z_1} = \frac{I_c}{2\pi\sqrt{(b_c+\rho_1)^2+(z+h_c)^2}}\left[K + \frac{b_c^2-\rho_1^2-(z+h_c)^2}{(b_c-\rho_1)^2+(z+h_c)^2}E\right], \quad (4.5)$$

where K and E are complete elliptic integrals of first and second kind, respectively, with modulus $\sqrt{4b_c\rho_1/\left[(b_c+\rho_1)^2+(z+h_c)^2\right]}$. The inducing magnetic field intensity produced by the current-carrying turn, at the point of observation is

$$\boldsymbol{H}_{inc} = H_{inc}^{\rho_1}\sin\upsilon\hat{\boldsymbol{x}} - H_{inc}^{\rho_1}\cos\upsilon\hat{\boldsymbol{y}} + H_{inc}^{z_1}\hat{\boldsymbol{z}}, \quad (4.6)$$

with $\sin\upsilon = \rho\cos\phi/\rho_1$ and $\cos\upsilon = (d_c - \rho\sin\phi)/\rho_1$. Therefore, the inducing field matrix elements are computed from (2.34) with

$$H_{inc,n}^{t}(t_i) = \frac{-1}{2\pi}\int_0^{2\pi}(H_{inc}^{\rho_1}\sin\upsilon\sin\phi + H_{inc}^{\rho_1}\cos\upsilon\cos\phi)e^{-jn\phi}d\phi \quad (4.7)$$

$$H_{inc,n}^{\phi}(t_i) = \frac{-1}{2\pi}\int_0^{2\pi}(H_{inc}^{\rho_1}\sin\upsilon\sin\alpha\cos\phi - H_{inc}^{\rho_1}\cos\upsilon\sin\alpha\sin\phi + H_{inc}^{z_1}\cos\alpha)e^{-jn\phi}d\phi, \quad (4.8)$$

where $H_{inc}^{\rho_1}$, $H_{inc}^{z_1}$, $\sin\upsilon$ and $\cos\upsilon$ are evaluated at $t = t_i$. For each Fourier mode $[n \in (-\infty, \infty)]$, the integrals in (4.7) and (4.8) are evaluated numerically.

4.2.2 Results for Spheres

Unlike in all the other examples presented so far, the Fourier series expansion of the inducing field produced by the circular current-carrying turn, with its axis shifted with respect to the body's axis of symmetry, is an infinite series. In all the cases considered in this section, the results are computed with 25 meridian segments.

The effect of truncating the Fourier series is investigated for various ratios of a_s/b_c and d_c/a_s while keeping $h_c/b_c = 1$. Figure 4.6 shows the percentage error with respect to the maximum value of the normalized tangential magnetic field calculated with various number n of Fourier modes, $|n| < 10$, with respect to the corresponding value calculated with Fourier modes n from -10 to 10. When $n = \pm 4$, i.e. when only the modes from -4 to 4 are used to calculate the tangential magnetic field, the absolute percentage error is already practically zero. It can be also seen from Fig. 4.6 that the mode $n = 0$ gives results with significant accuracy (absolute percentage error less than 0.25%) for small shifts in the turn axis ($d_c/a_s \leq 0.1$).

On the other hand, the results generated with $n = \pm 4$ and 25 meridian segments show a very good accuracy as compared to those generated with 50 segments. The absolute percentage error between the two sets of results is less than 0.3% for all the cases tested.

The normalized magnetic field on the surface of a sphere in the presence of a circular turns of different sizes placed at different locations is shown in Fig. 4.7. The tangential magnetic field is normalized with respect to I_c/a_s. The results from the exact solution are also shown for the coaxial turn case. For small shifts of the turn axis with respect to the $z-$axis, the results are close to those for the coaxial case, except near the poles.

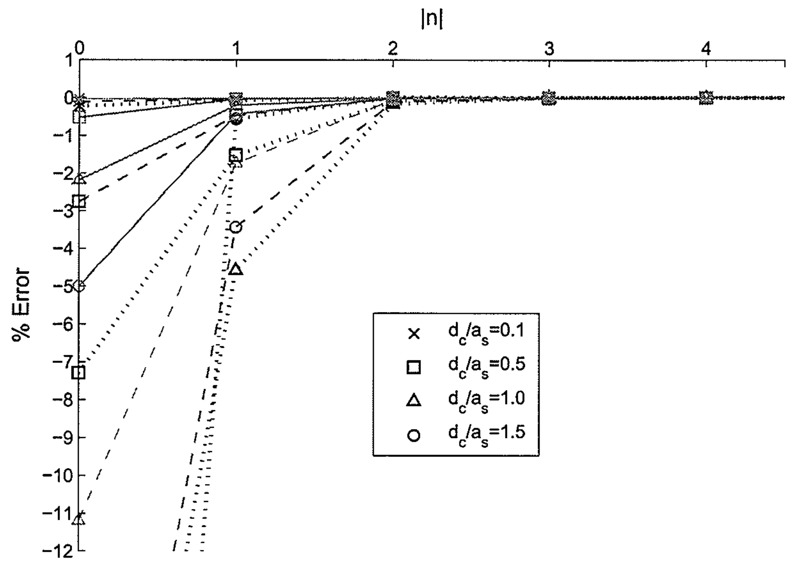

Figure 4.6: Effect of number of Fourier modes on the convergence of the maximum normalized magnetic field for a sphere in the presence of a current-carrying turn with $h_c/b_c = 1$, various d_c/a_s and a_s/b_c: $a_s/b_c = 0.25$ ——; $a_s/b_c = 0.5$ - - -; $a_s/b_c = 0.75 \cdots\cdot$.

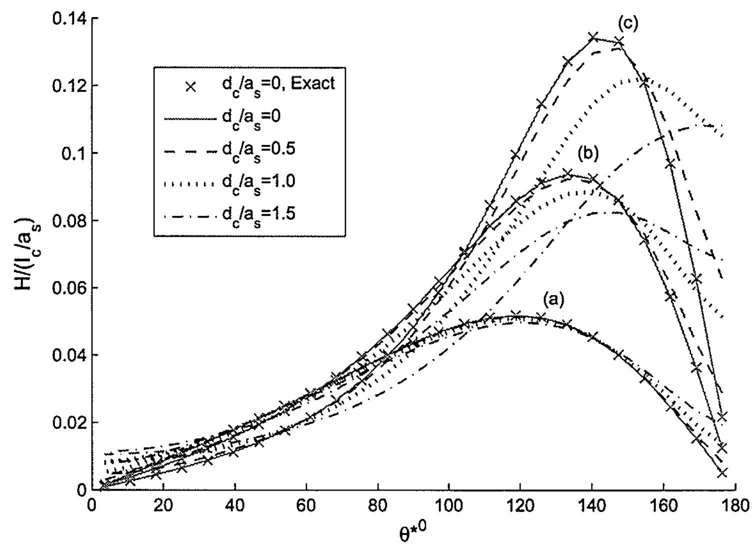

Figure 4.7: Normalized magnetic field at $\phi = 0^0$ for a sphere in the presence of a current-carrying turn with $h_c/b_c = 1$, various d_c/a_s and: (a)$a_s/b_c = 0.25$; (b)$a_s/b_c = 0.5$; (c)$a_s/b_c = 0.75$.

4.2.3 Results for Spheroids

As in the case of the sphere, only the Fourier modes up to $n = \pm 4$ are used to generate satisfactory results for conducting spheroids. There is no difference in the first 5 significant digits between these results and those obtained with the Fourier modes up to $n = \pm 10$. We use 25 meridian segments in all cases considered. The tangential magnetic field is normalized with respect to I_c/b_0 in case of the prolate spheroid and I_c/a_0 in case of the oblate spheroid.

Figures 4.8 and 4.9 show the normalized magnetic field at $\phi = 0^0$ for a prolate spheroid with an axial ratio of 1.25 and for an oblate spheroid with an axial ratio of 0.8, in the presence of a circular current-carrying turn of different sizes. The shift of the turn axis in the $y - z$ plane is varied by changing the ratio d_c/b_0 while keeping $h_c/b_c = 1$. The results corresponding to the exact solution for a coaxial turn are also shown for both types of spheroids.

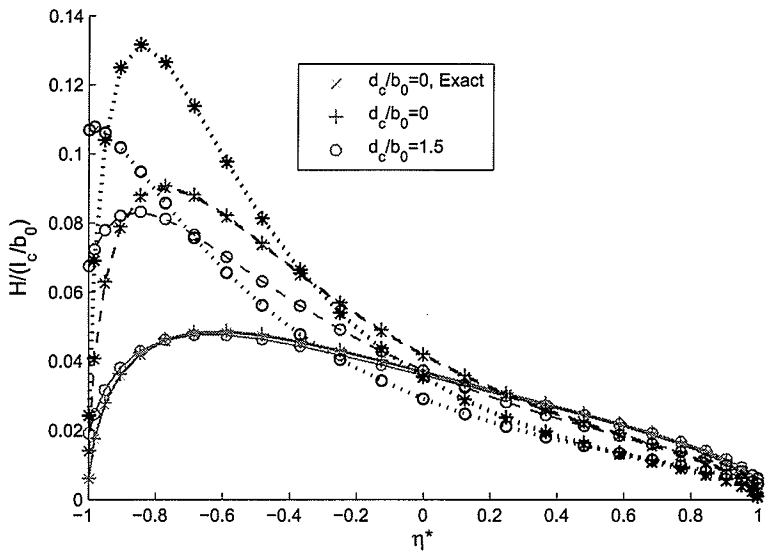

Figure 4.8: Normalized magnetic field at $\phi = 0^0$ for a prolate spheroid with $a_0/b_0 = 1.25$ in the presence of a current-carrying turn with $h_c/b_c = 1$, various d_c/b_0 and b_0/b_c: $b_0/b_c = 0.25$ ——; $b_0/b_c = 0.5$ - - - ; $b_0/b_c = 0.75 \cdots\cdot$.

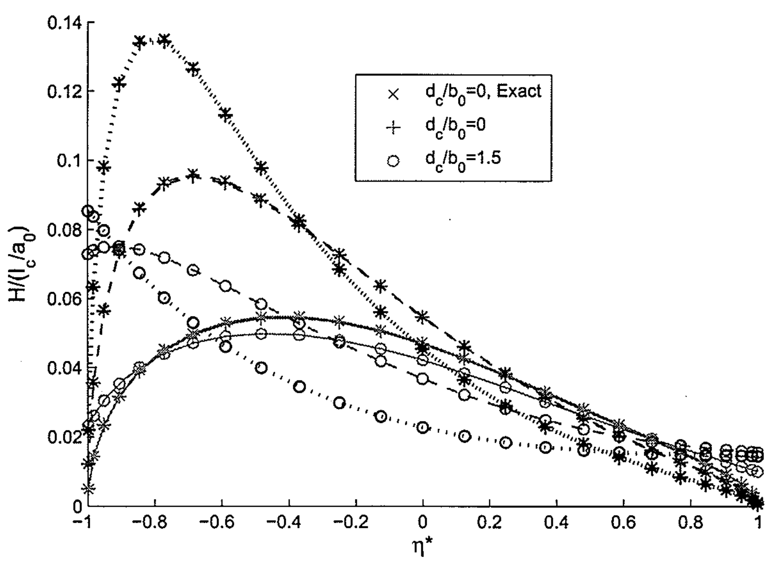

Figure 4.9: Normalized magnetic field at $\phi = 0^0$ for an oblate spheroid with $a_0/b_0 = 0.8$ in the presence of a current-carrying turn with $h_c/b_c = 1$, various d_c/b_0 and a_0/b_c: $a_0/b_c = 0.25$ ——; $a_0/b_c = 0.5$ - - - ; $a_0/b_c = 0.75 \cdots\cdot$.

Chapter 5

Conclusion and Future Work

In this thesis, an efficient analysis of the magnetic field produced by arbitrary quasistationary inducing fields in the presence of axisymmetric conducting bodies is presented. An integral equation is formulated for the induced surface current density on the conductor surface under the assumption of a negligible depth of penetration of the fields into the conductor. The field quantities on the surfaces of the conductors are expressed in terms of the meridian and azimuthal coordinates in the form of Fourier series in the azimuthal angle. For computing numerical results, the integral equation is converted into a matrix equation by applying the method of moments.

The efficiency of using pulse basis functions instead of impulse basis functions is shown when calculating the induced surface current densities of a prolate spheroid in the presence of an axially directed uniform magnetic field. It has been noticed that about twice the number of meridian segments needs to be used when using impulse basis functions, to achieve the same accuracy as given by the pulse basis functions. The numerical results are generated for the normalized tangential magnetic field intensity on the surface of both prolate and oblate spheroids, as well as the surface of spheres, in the presence of axially directed uniform magnetic fields and coaxial circular current-carrying turns. They are compared with the results generated from exact analytical formulations using the PEC model. For spheres the computed results are in good agreement with the exact results (absolute percentage error less than 0.6%). It is noticed that for conducting spheroids the relative error between the numerical results generated by the method of moments and the exact results increases as the axial ratio increases for prolate spheroids and as it decreases for oblate spheroids, especially at points near the spheroid poles.

The numerical computation performed for conducting spheroids and spheres in uniform fields arbitrarily oriented and in the fields from current-carrying circular turns whose axes are shifted from the axis of revolution of the spheroids show the high efficiency of the method employed. The Fourier series expansion converges rapidly and only Fourier modes up to $n = \pm 4$ are sufficient to generate results accurate to five significant digits as compared to the results generated with Fourier modes up to $n = \pm 10$. Also, the generated numerical results for the spheres in arbitrarily oriented uniform fields are in good agreement with the analytical results (absolute percentage error less than 1% in all the cases considered).

5.1 Future Work

Pulse basis functions yields more accurate results for the normalized tangential magnetic field intensity in the case of spheres and in the case of spheroids with axial ratios close to unity. Performance of the method presented in this thesis needs to be investigated by using other types of weighting and basis functions in order to improve the overall efficiency, especially for very elongated prolate spheroids and flat oblate spheroids, and for the regions in the neighborhood of the poles. The efficiency of using smaller lengths for segments closer to the poles than for those at the middle of the meridian should also be investigated.

The results obtained for the normalized tangential magnetic field on the surface of spheroids in the presence of an arbitrarily directed uniform fields and in the presence of a coil with its axis shifted with respect to the body's axis of revolution should be compared with results obtained by other methods, for instance, the existing method based on discretizing the entire surface of the conducting bodies.

In this thesis we have considered only objects with smooth boundaries. It will be useful to investigate the performance of the method presented in this thesis for conductors with sharp edges and vertices.

Furthermore, the formulation in this thesis can be extended for conducting bodies of revolution at low frequencies to take into account the penetration of fields inside the bodies.

Appendix A

Exact Solutions for Perfect Conducting Spheroids in Axisymmetric Fields

A.1 Spheroids in the Presence of Coaxial Current-Carrying Turns

For a prolate spheroid in the presence of a coaxial circular current-carrying turn as shown in Fig. 3.10, the magnetic vector potential outside the body is in the direction of $\hat{\boldsymbol{\phi}}^*$, due to the axisymmetry of the system. Also, it is independent of ϕ^*. Therefore, the magnetic vector potential can be written as

$$\boldsymbol{A}(\eta^*, \xi^*) = \hat{\boldsymbol{\phi}}^* A(\eta^*, \xi^*), \tag{A.1}$$

which satisfies the vector Laplace equation. A solution for the magnetic vector potential outside can be found by superposing the solutions for two different problems,

$$\nabla^2 \boldsymbol{A}' = 0 \text{ and} \tag{A.2}$$

$$\nabla^2 \boldsymbol{A}'' = \mu_0 \boldsymbol{J}_{s,\,c}. \tag{A.3}$$

The current density in the circular turn carrying the current I_c is expressed as

$$\boldsymbol{J}_{s,\,c} = \frac{I_c \delta(\eta^* - \eta_c^*)\delta(\xi^* - \xi_c^*)\sqrt{(1-\eta_c^{*2})\,(\xi_c^{*2}-1)}}{c^2(\xi_c^{*2} - \eta_c^{*2})}, \tag{A.4}$$

where η_c^*, ξ_c^* are the coordinates of the circular turn and δ is the Dirac delta function. The coordinates η_c^* and ξ_c^* are related to the radius of the circular turn b_c and the vertical distance to the center of the turn from the origin of the (x, y, z) coordinate system as

$$d_c + a_0 = c\eta_c^*\xi_c^*, \qquad b_c = c\sqrt{(1-\eta_c^{*2})(\xi_c^{*2}-1)}. \tag{A.5}$$

The solution of (A.2) in prolate spheroidal coordinates defined in (3.3) is given by the method of separation of variables in the form

$$A' = \sum_{p=1}^{\infty} C_p Q_p^1(\xi^*) P_p^1(\eta^*), \tag{A.6}$$

where P_p^1 and Q_p^1 are associated Legendre functions of the first and second kind, respectively, and C_p are constants of integration. A particular solution of (A.3) can be obtained from the volume integral

$$\boldsymbol{A}'' = \frac{\mu_0}{4\pi}\int_v \frac{\boldsymbol{J}_{s,\,c}}{|\boldsymbol{r} - \boldsymbol{r}'|} dv', \tag{A.7}$$

where $\boldsymbol{r}$ and $\boldsymbol{r}'$ are the position vectors of the observation and source points, respectively. Substituting (A.4) into (A.7) and expanding $1/|\boldsymbol{r} - \boldsymbol{r}'|$ in terms of prolate spheroidal harmonics [7] yields

$$A'' = -\frac{\mu_0 I_c}{2}\sqrt{(1-\eta_c^{*2})\,(\xi_c^{*2}-1)}\sum_{p=1}^{\infty}\frac{2p+1}{[p(p+1)]^2} P_p^1(\xi_<^*) Q_p^1(\xi_>^*) P_p^1(\eta_c^*) P_p^1(\eta^*), \tag{A.8}$$

where $\xi_<^*$ and $\xi_>^*$ are the smallest and the largest of ξ^* and ξ_c^*, respectively. Thus, the total magnetic vector potential outside the body is

$$\begin{aligned} A =& \sum_{p=1}^{\infty} C_p Q_p^1(\xi^*) P_p^1(\eta^*) \\ &- \frac{\mu_0 I_c}{2} \sqrt{(1-\eta_c^{*2})(\xi_c^{*2}-1)} \sum_{p=1}^{\infty} \frac{2p+1}{[p(p+1)]^2} P_p^1(\xi_<^*) Q_p^1(\xi_>^*) P_p^1(\eta_c^*) P_p^1(\eta^*). \end{aligned} \tag{A.9}$$

The constants of integration are computed by imposing the condition $A = 0$ on the surface of the perfect conducting spheroid, i.e. at $\xi^* = \xi_0^*$. Finally, substituting the calculated value for C_p, the magnetic vector potential outside the perfect conducting prolate spheroid can be written as

$$\begin{aligned} A =& \frac{\mu_0 I_c}{2} \sqrt{(1-\eta_c^{*2})(\xi_c^{*2}-1)} \sum_{p=1}^{\infty} \frac{2p+1}{[p(p+1)]^2} \\ &\cdot \left[\frac{P_p^1(\xi_0^*)}{Q_p^1(\xi_0^*)} Q_p^1(\xi_c^*) Q_p^1(\xi^*) - P_p^1(\xi_<^*) P_p^1(\xi_>^*) \right] P_p^1(\eta_c^*) P_p^1(\eta^*). \end{aligned} \tag{A.10}$$

With prolate to oblate spheroidal transforms given in Chapter 3, the magnetic vector potential for an oblate spheroid is

$$\begin{aligned} A =& \frac{j\mu_0 I_c}{2} \sqrt{(1-\eta_c^{*2})(\xi_c^{*2}+1)} \sum_{p=1}^{\infty} \frac{2p+1}{[p(p+1)]^2} \\ &\cdot \left[\frac{P_p^1(j\xi_0^*)}{Q_p^1(j\xi_0^*)} Q_p^1(j\xi_c^*) Q_p^1(j\xi^*) - P_p^1(j\xi_<^*) P_p^1(j\xi_>^*) \right] P_p^1(\eta_c^*) P_p^1(\eta^*). \end{aligned} \tag{A.11}$$

The magnetic flux density outside the prolate spheroid can be determined by taking the curl of the magnetic vector potential. Thus, the magnetic field intensity outside is obtained from

$$\begin{aligned} H_{\eta^*} &= \frac{1}{\mu_0 h_{\xi^*} h_{\phi^*}} \frac{\partial}{\partial \xi^*} (h_{\phi^*} A) \\ H_{\xi^*} &= -\frac{1}{\mu_0 h_{\eta^*} h_{\phi^*}} \frac{\partial}{\partial \eta^*} (h_{\phi^*} A). \end{aligned} \tag{A.12}$$

On the surface of a perfect conductor only the tangential component of the magnetic field is present. Therefore, at $\xi^* = \xi_0^*$, for a prolate spheroid

$$H_{\eta^*} = \frac{I_c}{2c}\left[\frac{(1-\eta_c^{*2})(\xi_c^{*2}-1)}{(\xi_0^{*2}-\eta^{*2})(\xi_0^{*2}-1)}\right]^{1/2}\sum_{p=1}^{\infty}\frac{2p+1}{p(p+1)}\frac{Q_p^1(\xi_c^*)}{Q_p^1(\xi_0^*)}P_p^1(\eta_c^*)P_p^1(\eta^*). \tag{A.13}$$

and for an oblate spheroid

$$H_{\eta^*} = \frac{I_c}{2c}\left[\frac{(1-\eta_c^{*2})(\xi_c^{*2}+1)}{(\xi_0^{*2}+\eta^{*2})(\xi_0^{*2}+1)}\right]^{1/2}\sum_{p=1}^{\infty}\frac{2p+1}{p(p+1)}\frac{Q_p^1(j\xi_c^*)}{Q_p^1(j\xi_0^*)}P_p^1(\eta_c^*)P_p^1(\eta^*). \tag{A.14}$$

A.2 Special Cases

Axially directed uniform field

By letting $\xi_c^* \to \infty$ and by taking into account the asymptotic expansions for large arguments of the associated Legendre functions in (A.10) and (A.11) , the magnetic vector potential for a prolate spheroid can be found as [7]

$$A = \mu_0 H_{inc}\frac{c}{2}\sqrt{(1-\eta^{*2})\,(\xi^{*2}-1)}\left[1-\frac{\ln\dfrac{\xi^*+1}{\xi^*-1}-\dfrac{2\xi^*}{\xi^{*2}-1}}{\ln\dfrac{\xi_0^*+1}{\xi_0^*-1}-\dfrac{2\xi_0^*}{\xi_0^{*2}-1}}\right] \tag{A.15}$$

and

$$A = \mu_0 H_{inc}\frac{c}{2}\sqrt{(1-\eta^{*2})\,(\xi^{*2}+1)}\left[1-\frac{\cot^{-1}\xi^*-\dfrac{\xi^*}{\xi^{*2}+1}}{\cot^{-1}\xi_0^*-\dfrac{\xi_0^*}{\xi_0^{*2}+1}}\right] \tag{A.16}$$

in the case of an oblate spheroid, where, H_{inc} is the inducing uniform magnetic field which is given by

$$H_{inc} = \frac{1}{2c}\lim_{I_c,\xi_c^*\to\infty}\frac{I_c(1-\eta_c^{*2})}{\xi_c^*}. \tag{A.17}$$

From (A.12), the tangential magnetic field on the surface is

$$H_{\eta^*} = \frac{-2H_{inc}}{(\xi_0^{*2}-1)\ln\dfrac{\xi_0^*+1}{\xi_0^*-1}-2\xi_0^*}\left[\frac{1-\eta^{*2}}{\xi_0^{*2}-\eta^{*2}}\right]^{1/2} \tag{A.18}$$

for a prolate spheroid and

$$H_{\eta^*} = \frac{H_{inc}}{(\xi_0^{*2}+1)\cot^{-1}\xi_0^* - \xi_0^*}\left[\frac{1-\eta^{*2}}{\xi_0^{*2}+\eta^{*2}}\right]^{1/2} \tag{A.19}$$

for an oblate spheroid.

Sphere in the presence of a coaxial current-carrying turn

Using the asymptotic expansions for large arguments of the associated Legendre functions and the prolate spheroidal to spherical transforms given in Chapter 3, the magnetic vector potential for the case of a sphere is found to be

$$A = \frac{\mu_0 I_c \sin\theta_c^*}{2}\sum_{p=1}^{\infty}\frac{1}{p(p+1)}\left[\frac{r_<^{*p}}{r_>^{*p+1}}r_c^* - \left(\frac{a_s}{r_c^*}\right)^p\left(\frac{a_s}{r^*}\right)^{p+1}\right]P_p^1(\cos\theta_c^*)P_p^1(\cos\theta^*), \tag{A.20}$$

where $r_<^*$ and $r_>^*$ are the smallest and the largest of r^* and r_c^*, respectively. Here, r_c^* and θ_c^* are the coordinates of the circular turn in circular cylindrical coordinates and a_s is the radius of the sphere.

The tangential component of the magnetic field intensity on the sphere surface can be found from the curl of the magnetic vector potential as

$$H_{\theta^*} = \frac{I_c\sin\theta_c^*}{2a_s}\sum_{p=1}^{\infty}\frac{(2p+1)}{p(p+1)}\left(\frac{a_s}{r_c}\right)^p P_p^1(\cos\theta_c^*)P_p^1(\cos\theta^*). \tag{A.21}$$

Appendix B

Exact Solution for a Sphere in a Uniform Field Directed at an Angle with Respect to the z-Axis

The magnetic field both inside and outside of a conducting sphere in an axially directed uniform field can be determined by using the method of separation of variables. The magnetic flux density outside a conducting sphere with resistivity σ, permeability μ and radius a_s, placed in a uniform alternating $z-$ directed magnetic field of flux density B_0 is given by [12]

$$\boldsymbol{B} = B_0 \left[\hat{\boldsymbol{r}}^* \left(1 + \frac{D_0}{r^{*3}} \right) \cos\theta^* - \hat{\boldsymbol{\theta}}^* \left(1 - \frac{D_0}{2r^{*3}} \right) \sin\theta^* \right], \tag{B.1}$$

where θ^* is the meridian angle with respect to the sphere center and r^* the distance from the center of the observation point, and

$$D_0 = \frac{(2\mu + \mu_0)\gamma a I_{-1/2} - \{\mu_0[1 + (\gamma a)^2] + 2\mu\} I_{1/2}}{(\mu - \mu_0)\gamma a I_{-1/2} + \{\mu_0[1 + (\gamma a)^2] - \mu\} I_{1/2}} a_s^3. \tag{B.2}$$

Here, $\gamma = \sqrt{j\sigma\omega\mu}$ and $I_{\pm 1/2}$ are modified Bessel functions of the first kind with the argument γa. At very high frequency, the magnetic field intensity on the surface of the sphere is given by

$$\boldsymbol{H} = -1.5 H_0 \sin\theta^* \, \hat{\boldsymbol{\theta}}^*, \tag{B.3}$$

where $\hat{\boldsymbol{\theta}}^{*}$ is the unit vector along the meridian angle and $H_0 = B_0/\mu_0$.

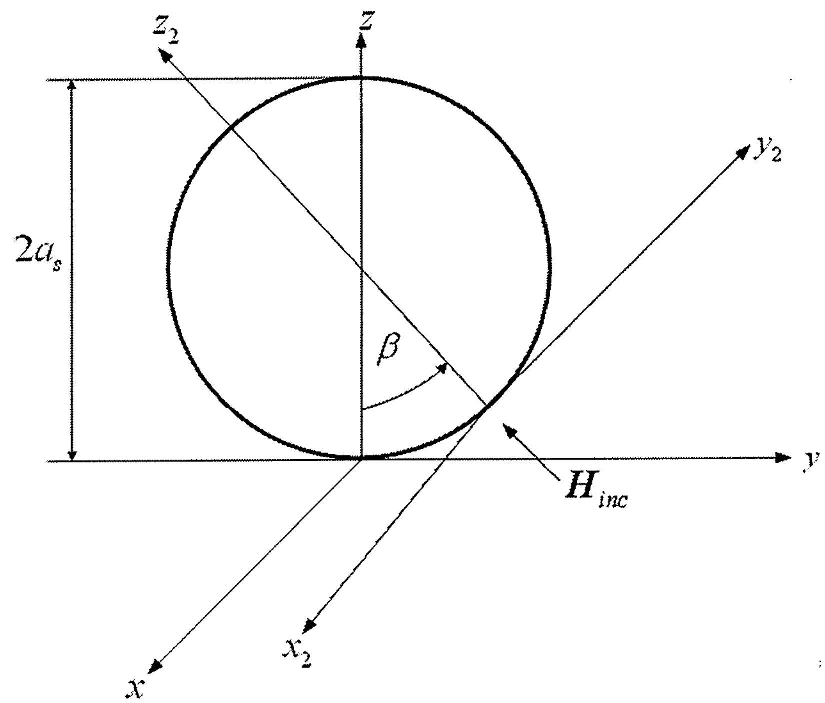

Figure B.1: Sphere in a uniform magnetic field directed at an angle β with respect to the z-axis.

For a sphere in a uniform inducing field directed at an angle β with respect to the z-axis, as shown in Fig. B.1, the inducing field can be expressed as $\boldsymbol{H}_{inc} = H_{inc}(-\hat{\boldsymbol{y}}\sin\beta + \hat{\boldsymbol{z}}\cos\beta)$. We use a rotation and a translation of the coordinate system such that the new z-axis be aligned with the direction of the inducing field. The relationship between the (x, y, z) system and the new (x_2, y_2, z_2) system is

$$\begin{aligned} \hat{\boldsymbol{x}}_2 &= \hat{\boldsymbol{x}}, \\ \hat{\boldsymbol{y}}_2 &= \hat{\boldsymbol{y}}\cos\beta + \hat{\boldsymbol{z}}\sin\beta, \\ \hat{\boldsymbol{z}}_2 &= -\hat{\boldsymbol{y}}\sin\beta + \hat{\boldsymbol{z}}\cos\beta, \end{aligned} \tag{B.4}$$

$$
\begin{aligned}
x &= x_2, \\
y &= a_s \sin\beta + y_2 \cos\beta - z_2 \sin\beta, \\
z &= a_s(1-\cos\beta) + y_2 \sin\beta + z_2 \cos\beta.
\end{aligned}
\tag{B.5}
$$

Then, the tangential magnetic field intensity on the surface of the body is obtained from (B.3) in the form

$$
\boldsymbol{H} = -1.5 H_0 \sin\theta_2 \, \hat{\boldsymbol{\theta}}_2, \tag{B.6}
$$

where $\theta_2 = \cos^{-1}(-\sin\alpha\cos\beta)$. With (B.4) and (2.24), for observation points at $\phi = 0^0$ on the surface of the sphere, we have

$$
\begin{aligned}
\hat{\boldsymbol{\theta}}_2 =& \hat{\boldsymbol{t}}(\cos\theta_2\cos\phi_2\sin\alpha + \cos\theta_2\sin\phi_2\cos\alpha\sin\beta - \sin\theta_2\cos\alpha\cos\beta) \\
&+ \hat{\boldsymbol{\phi}}(\cos\theta_2\sin\phi_2\sin\beta + sin\theta_2\sin\beta),
\end{aligned}
\tag{B.7}
$$

where α is the angle between the unit vectors $\hat{\boldsymbol{z}}$ and $\hat{\boldsymbol{t}}$ (see section 2.3), $\cos\phi_2 = \cos\alpha/\sqrt{\cos^2\alpha + \sin^2\alpha\sin^2\beta}$ and $\sin\phi_2 = -\sin\alpha\sin\beta/\sqrt{\cos^2\alpha + \sin^2\alpha\sin^2\beta}$.

Bibliography

[1] J. R. Wait, "A conducting permeable sphere in the presence of a coil carrying an oscillating current," *Can. J. Phys.*, vol. 31, pp. 670–678, 1953.

[2] K. A. S. N. Jayasekera and I. R. Ciric, "Benchmark computations of the fields, losses and forces for conducting spheroids in the proximity of current carrying turns," *IEEE. Trans. Magn.*, vol. 42, no. 7, pp. 1802–1811, July 2006.

[3] H. Braunisch, C. O. Ao, K. ONeill, and J. A. Kong, "Magnetoquasistatic response of conducting and permeable prolate spheroid under axial excitation," *IEEE Trans. Geosci. Remote Sensing*, vol. 30, no. 12, pp. 2689–2701, Dec. 2001.

[4] C. O. Ao, H. Braunisch, K. ONeill, and J. A. Kong, "Quasi-magnetostatic solution for a conducting and permeable spheroid with arbitrary excitation," *IEEE Trans. Geosci. Remote Sensing*, vol. 40, no. 4, pp. 887–897, Apr. 2002.

[5] K. A. S. N. Jayasekera and I. R. Ciric, "On the limits of validity of the impedance boundary conditions for the analysis of induced currents in solid conductors," in *Proc. Int. Symp. Antenna Technology and Applied Electromagnetics (ANTEM)*, Ottawa, ON, Canada, 2004, pp. 501–504.

[6] ——, "Evaluation of surface impedance models for axisymmetric eddy-current fields," *IEEE. Trans. Magn.*, vol. 43, no. 5, pp. 1191–2000, May 2007.

[7] I. R. Ciric, "Electromagnetic levitation in axially symmetric systems," *Rev. Roum. Sci. Techn. - Electrotechn. et Energ.*, vol. 15, pp. 35–73, 1970.

[8] M. N. Sadiku, *Numerical techniques in electromagnetics*, 2nd ed. Boca Raton, Florida: CRC Press, 2001.

[9] R. F. Harrington, "Matrix methods for field problems," in *Proc. IEEE*, 1967, pp. 136–149.

[10] ——, *Field computation by moment methods.* New York: Macmillan, 1968.

[11] J. R. Mautz and R. F. Harrington, "Radiation and scattering from bodies of revolution," *Appl. Sci. Res.*, vol. 20, pp. 405–435, June 1969.

[12] W. R. Smythe, *Static and dynamic electricity*, 3rd ed. New York: McGraw-Hill,Inc., 1968.

[13] M. Abromowitz and I. A. Stegun, *Handbook of Mathematical Functions with Formulas, Graphs and Mathematical Tables.* New York: Dover, 1970.

[14] W. Gautschi, "Algorithm 259, legendre functions for arguments larger than one," *Communications of the ACM*, vol. 8, no. 8, pp. 488–493, Aug. 1965.

[15] B. Barrowes. Matlab routines for computation of special functions. [Online]. Available: http://ceta.mit.edu/ceta/comp_spec_func/

[16] K. A. S. N. Jayasekera, "Performance analysis of the impedence boundary conditions for axisymmetric eddy current problems," Master's thesis, University of Manitoba, 2003.